NEUROSCIENCE

Reversal of hyperactive higher-order thalamus attenuates defensiveness in a mouse model of PTSD

Kaiwen Xi[1]†, Haoxiang Xiao[1]†, Xin Huang[1]†, Ziduo Yuan[1,2]†, Mingyue Liu[1,2], Honghui Mao[1], Haiying Liu[1], Guaiguai Ma[1,2], Zishuo Cheng[1], Yuqiao Xie[1], Yang Liu[1], Dayun Feng[3], Wenting Wang[1], Baolin Guo[1]*, Shengxi Wu[1]*

Posttraumatic stress disorder (PTSD) is a highly prevalent and debilitating psychiatric disease often accompanied by severe defensive behaviors, preventing individuals from integrating into society. However, the neural mechanisms of defensiveness in PTSD remain largely unknown. Here, we identified that the higher-order thalamus, the posteromedial complex of the thalamus (PoM), was overactivated in a mouse model of PTSD, and suppressing PoM activity alleviated excessive defensive behaviors. Moreover, we found that diminished thalamic inhibition derived from the thalamic reticular nucleus was the major cause of thalamic hyperactivity in PTSD mice. Overloaded thalamic innervation to the downstream cortical area, frontal association cortex, drove abnormal defensiveness. Overall, our study revealed that the malfunction of the higher-order thalamus mediates defensive behaviors and highlighted the thalamocortical circuit as a potential target for treating PTSD-related overreactivity symptoms.

INTRODUCTION

Posttraumatic stress disorder (PTSD) is a refractory mental illness often caused by severe accidents or disasters (*1*). The lifetime prevalence of PTSD worldwide is 1.9 to 6.8%, and 40% of the patients fail to respond to traditional exposures or pharmacological therapy (*2*). The lack of proper treatment of the disease affecting a vast number of patients places a tremendous economic and ethical burden on society (*1*). Thus, exploring the underlying pathological mechanisms and identifying reliable therapeutic targets are urgently needed.

Clinically, PTSD patients often exhibit excessive defensive responses to relatively minor stimulations, manifesting provoked behaviors and experiencing recurrent painful memories of involuntary and invasive traumatic events (*1*). Excessive defensive behaviors in people with PTSD lead to the inability to communicate appropriately, severely affecting their social lives and causing high suicide rates (*3*). However, the neural substrates of PTSD-related defensiveness remain underexplored.

Defensive behavior in animals refers to the conduct of dealing with foreign aggression and defending their survival to reduce the harm from other animals and guarantee the continuation of their species (*4*). Disproportionate defensive behaviors are commonly observed in many psychiatric disorders, which could cause an array of behavioral abnormalities, including antisocial behaviors and anxiety (*5*). In preclinical studies, freezing, flight, and aggressiveness to threats have been studied in rodents as defensive behaviors (*6*). Many studies have identified the amygdala and midbrain regions as critical areas encoding defensive behaviors (*7*), while recent evidence has revealed a distinct role of the thalamus in defensiveness and fear-associated learning (*8*). Moreover, clinical imaging studies have implicated the malfunction of the thalamus in many psychiatric disorders, including PTSD (*9*). However, whether the thalamic abnormalities are the underlying mechanisms of PTSD-related defensiveness remains unknown.

The thalamic nuclei could be classified into first-order thalamus and higher-order (HO) thalamus defined by driver inputs (*10*). By investigating the auditory system, pioneering research has identified the critical role of HO thalamic nuclei in threat cognition and defensive behaviors through top-down afferents (*8*). The somatosensory information is one of the most critical resources for receiving environmental stimulation and perceived external threats (*11*). However, it remains unclear whether the function of the somatosensory HO thalamic region, the posteromedial complex of the thalamus (PoM), is involved in elevated PTSD defensive behaviors. Furthermore, the inhibitory inputs from the thalamic reticular nucleus (TRN) and extrathalamic inhibitory system including zona incerta (ZI) and lateral hypothalamus, which regulate the thalamic activity (*10*, *12*), have been demonstrated to be associated with multiple psychiatric disorders such as schizophrenia (SCZ) (*13*), autism spectrum disorder (ASD) (*14*), and attention deficit and hyperactivity disorder (ADHD) (*15*). In addition, ZI, one of the most critical components of extrathalamic inhibitory system, and TRN have been reported to be relevant to defensive behaviors (*16*). Therefore, it was worthwhile studying whether abnormal thalamic inhibition contributes to PTSD-related defensive behaviors.

In this study, we used a modified single prolonged stress and electric foot shock (SPS&S) mouse model to observe excessive defensive behaviors in PTSD mice. By immediate early gene staining and in vivo calcium imaging, we found the hyperactivity of PoM in PTSD mice. Inhibiting PoM activity could alleviate defensiveness. In addition, by performing electrophysiological recordings, we identified that the impaired TRN inhibition caused hyperactivated PoM in PTSD mice. Activation of PoM, which receives projection from TRN, could rescue the PTSD-related behavioral abnormalities. Furthermore, by the targeted recombination in active populations

[1]Department of Neurobiology, School of Basic Medicine, Fourth Military Medical University, Xi'an 710032, China. [2]Medical School, Yan'an University, Yan'an 716000, China. [3]Department of Neurosurgery, Tangdu Hospital, Fourth Military Medical University, Xi'an 710032, China.
†These authors contributed equally to this work.
*Corresponding author. Email: baolguo@fmmu.edu.cn (B.G.); shengxi@fmmu.edu.cn (S.W.)

(TRAP) strategy, we provided evidence that the frontal association cortex (FrA) was downstream of PoM and accounted for defensiveness. Inhibiting the PoM-FrA pathway could decrease defensive responses in PTSD mice. Collectively, these results uncovered the role of PoM hyperactivity in PTSD-related defensiveness and highlighted the targeting manipulation for PTSD treatment based on circuit-level understandings of behavioral abnormalities.

RESULTS

PTSD mice exhibit excessive defensive behaviors

We examined defensive behaviors in PTSD mice by using an SPS&S mouse model, which could effectively mimic neural and behavioral characteristics of PTSD, as previously described (*17*). SPS&S mice received four consecutive stressors: restraint, forced swimming, deep anesthesia, and unconditioned foot shock (Fig. 1A). We first investigated the defensive behaviors provoked by a whisker stimulation, which could reflect innate defensive behavioral states induced by tactile-related threats. After habituation in the home cage for 35 min, each mouse received three consecutive 5-min manual whisker stimulation with a wooden applicator sticker with a 1-min interval for a break (Fig. 1B). The scoring criteria for defensive behaviors have been described before (*18*), which contained five parameters: freezing, stance, hyperventilation, aggression, and evasiveness. Each parameter had three scores from 0 to 2, and the total scores reflected the degree of defensive response. Compared with the control mice, PTSD mice showed significantly increased response scores (Fig. 1C and movie S1).

To explore the learned defensive behaviors associated with the environmental and auditory stimuli, we applied the contextual fear conditioning (CFC) test in PTSD mice with a pair of conditioned stimuli (CS) of tone (4500 Hz, 75 dB, 28 s) and unconditioned stimuli (US) of foot shock (0.6 mA, 2 s) (Fig. 1D). We used the freezing time of each mouse to measure the defensiveness. On the second day after training, PTSD mice showed elevated freezing time in chamber A with the trauma-related environment. Significantly, we also observed increased freezing behaviors on the seventh day after the training of PTSD mice (Fig. 1, E and F).

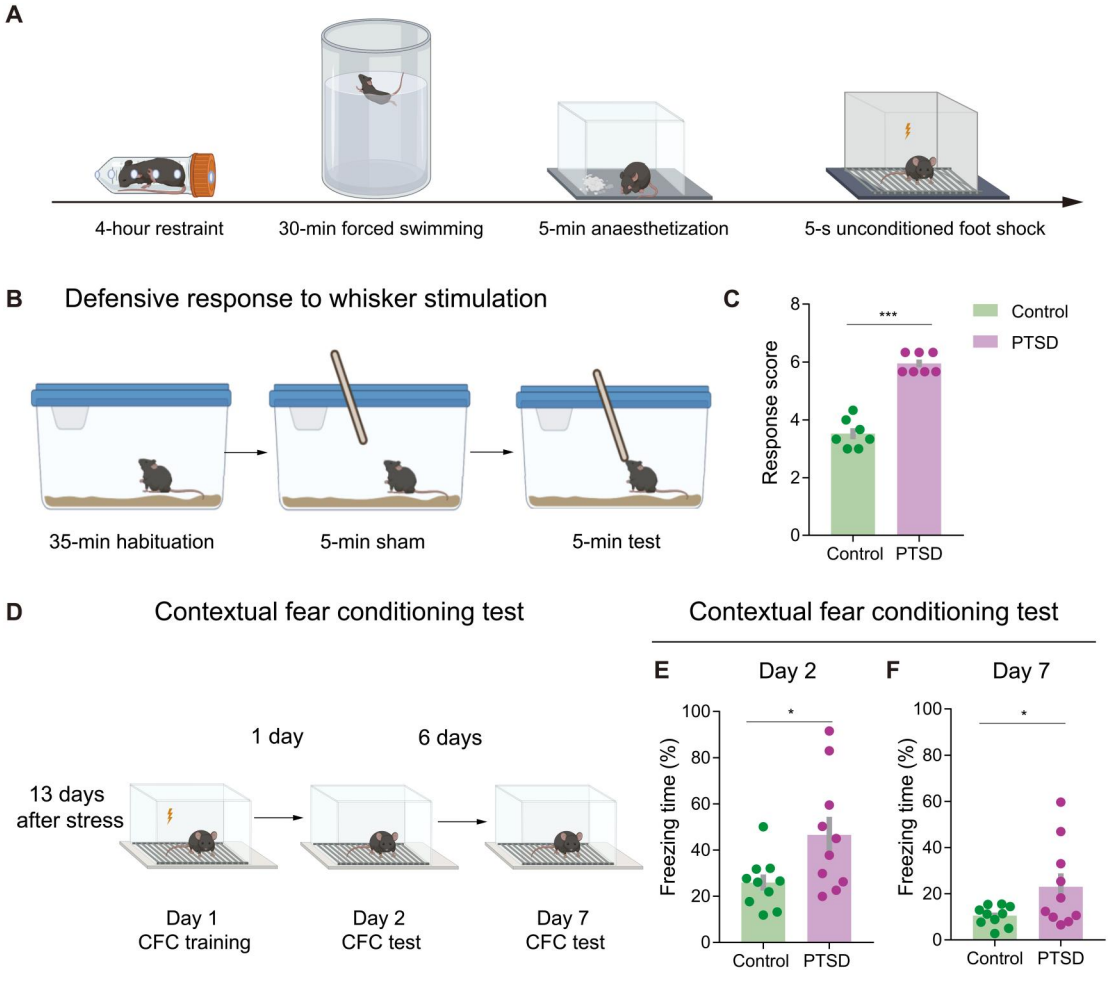

Fig. 1. PTSD mice show excessive defensive behavior. (**A**) Schematic of PTSD model establishment. (**B**) Schematic of the test for defensive response to whisker stimulation. (**C**) Response scores of total defensive behaviors in control and PTSD mice. Total response score was elevated in PTSD mice (n = 7 mice for each group). (**D**) Schematic of the contextual fear conditioning (CFC) test. (**E**) Freezing time in the day 2 CFC test. PTSD mice exhibited elevated freezing time in the day 2 CFC test. (**F**) Freezing time in the day 7 CFC test. PTSD mice exhibited elevated freezing time in the day 7 CFC test (n = 10 mice for each group). Data are presented as means ± SEM. *P < 0.05 and ***P < 0.001. See table S1 for detailed statistical information.

Besides, PTSD mice showed excessive defensive behaviors in response to CS of tone related to the traumatic experience in chamber B (fig. S1, A and B). To avoid the potential influence of locomotor activity on the defensiveness measurements, we tested the locomotion in the open field and did not observe significant changes on the total distance between groups (fig. S2). These results indicated that innate and learned defensive behaviors were significantly increased in PTSD mice.

PoM plays an essential role in defensive behaviors in PTSD mice

We tested the role of the somatosensory thalamus in the defensive behaviors by quantifying the expression of the cytoskeleton-associated protein (Arc), an immediate-early gene (*19*), in the HO thalamus, PoM, and first-order thalamus, ventral posterior medial (VPM) thalamic nuclei after the mice exhibited defensive behaviors in response to tactile threats (Fig. 2A). Microtubule-associated protein 2 (MAP2) was used as a marker to precisely label neuronal morphology (*20*). We observed increased neural activation in the PoM of PTSD mice (Fig. 2, B to G). By contrast, no significant changes in neural activity in VPM were observed between the PTSD and control mice (Fig. 2, B to G).

We performed fiber photometry of calcium signals to examine the PoM activation pattern in vivo while mice received environmental threats and observed the defensive behaviors simultaneously. We injected adeno-associated virus (AAV) encoding a genetically encoded calcium indicator, GCaMP6s, driven by the human synapsin promoter (hSyn), unilaterally into the PoM of PTSD and control mice. Subsequently, we implanted an optic fiber just above the PoM (Fig. 2, H and I). Calcium signals increased strongly and reliably when the mice actively defended while receiving a 1-s whisker stimulation by a fixed air puff (Fig. 2, K and L). The amplitude of calcium signals was higher in PTSD mice than in control mice (Fig. 2J). In addition, we put the mice into the traumatic environment (chamber A) and recorded calcium signals. The frequency of spontaneous calcium events in the PoM increased after CFC training in both groups (fig. S3, A to E). Moreover, the frequency of spontaneous calcium events in the PoM increased in PTSD mice in both day 2 CFC test and day 7 CFC test (Fig. 2, M to P). Thus, the PoM hyperactivity in PTSD mice was related to excessive defensive behaviors.

Inhibition of PoM neurons normalizes defensive behaviors in PTSD mice

Given the abnormal activation of PoM neurons in PTSD mice, we explored the causal link between PoM hyperactivity and defensive behaviors. First, we bilaterally injected AAV carrying the inward rectifier K^+ channel Kir2.1 combined with the enhanced green fluorescent protein (eGFP) for the long-term inhibition of the PoM neural activity (Fig. 3, A and B). The virus was allowed to express in the PoM of each mouse 1 week before they received PTSD stress. We tested the Kir2-mediated currents at the seventh day following virus injection and recorded enhanced Kir currents in the Kir2.1 overexpression group (fig. S4, A to E). We also measured the number of action potentials between groups and found that, with the same stimulation intensity, neurons in the Kir2.1 overexpression group showed decreased spike numbers compared to the eGFP group (fig. S4, F and G). Two weeks later, mice were exposed to whisker stimulation and environmental threats to provoke innate and learned defensive behaviors (Fig. 3C).

With Kir2.1 overexpression in PoM, the PTSD mice exhibited decreased innate defensive behaviors in response to tactile stimuli as compared with the eGFP control of PTSD mice (Fig. 3D). eGFP-expressing PTSD mice showed excessive learned defensive response to environmental stimuli on the 2nd and 7th day CFC test. In contrast, Kir2.1-expressing PTSD mice exhibited decreased learned defensive responses to environmental stimuli compared with eGFP-expressing PTSD mice. The defensive responses of Kir2.1-expressing PTSD mice could reach to the level of eGFP-expressing control mice (Fig. 3, E and F). However, when exposed to trauma-related auditory stimuli, Kir2.1-expressing PTSD mice showed little difference in freezing time compared with eGFP-expressing PTSD mice (fig. S5A).

Kir2.1 inhibition may also influence the PoM activity before introducing stressors, so we then chemogenetically inhibited PoM neural activity in a specific time window by injecting bilaterally AAV carrying hM4D(Gi) or mCherry (Fig. 3, G and H). Each mouse was intraperitoneally injected compound 21 (C21) at a concentration of 2 mg/kg 30 min before innate and learned defensive behavioral tests (Fig. 3I). We used Arc staining to validate the effects of DREADD (designer receptor exclusively activated by designer drugs) strategy and found that the hM4D(Gi) group showed decreased expression of Arc (fig. S6). The mCherry-expressing PTSD mice showed significantly higher scores in the total defensive response. On the other hand, the hM4D(Gi)-expressing PTSD mice exhibited reduced defensive responses after C21 injection. The total score was comparable to the level of mCherry-expressing control mice (Fig. 3J).

Next, we compared the learned defensive behaviors in chamber A on the 2nd and 7th day CFC test. C21 injection significantly reduced the freezing time of hM4D(Gi)-expressing PTSD mice in the traumatic environment compared with mCherry-expressing PTSD mice in 2nd and 7th day CFC test (Fig. 3, K and L). However, when injected with C21 and exposed to a neutral environment of chamber B with trauma-related auditory stimuli, we did not observe a significant improvement in the freezing time in hM4D(Gi)-expressing PTSD mice compared with mCherry-expressing control mice (fig. S5B). We confirmed the injection sites of all the animals after behavioral tests (fig. S7). These results demonstrated that the hyperactivity of PoM neurons was vital for the induction of defensiveness related to tactile and environmental threats in PTSD mice, and PoM inhibition could normalize the defensive behaviors in PTSD mice.

PoM neurons receive decreased inhibitory inputs from TRN in PTSD

Thalamic inhibition has been reported to regulate thalamic activity (*21*). We wondered whether thalamic inhibition changed in PTSD mice, so we further investigated the role of changed thalamic inhibition in PTSD with retrobead-based tracing and confirmed the primary upstream inhibitory sources of PoM, TRN, and ZI (fig. S8, A to D). We performed Arc immunostaining in glutamic acid decarboxylase 67 (GAD67)–GFP transgenic mice to visualize the GABAergic (γ-aminobutyric acid–releasing) neurons in TRN and ZI and observed fewer GFP^+Arc^+ neurons in the TRN in PTSD mice (Fig. 4, A to F) along the anterior (A) to posterior (P) axis (fig. S8, E to G). By contrast, we did not observe any difference in

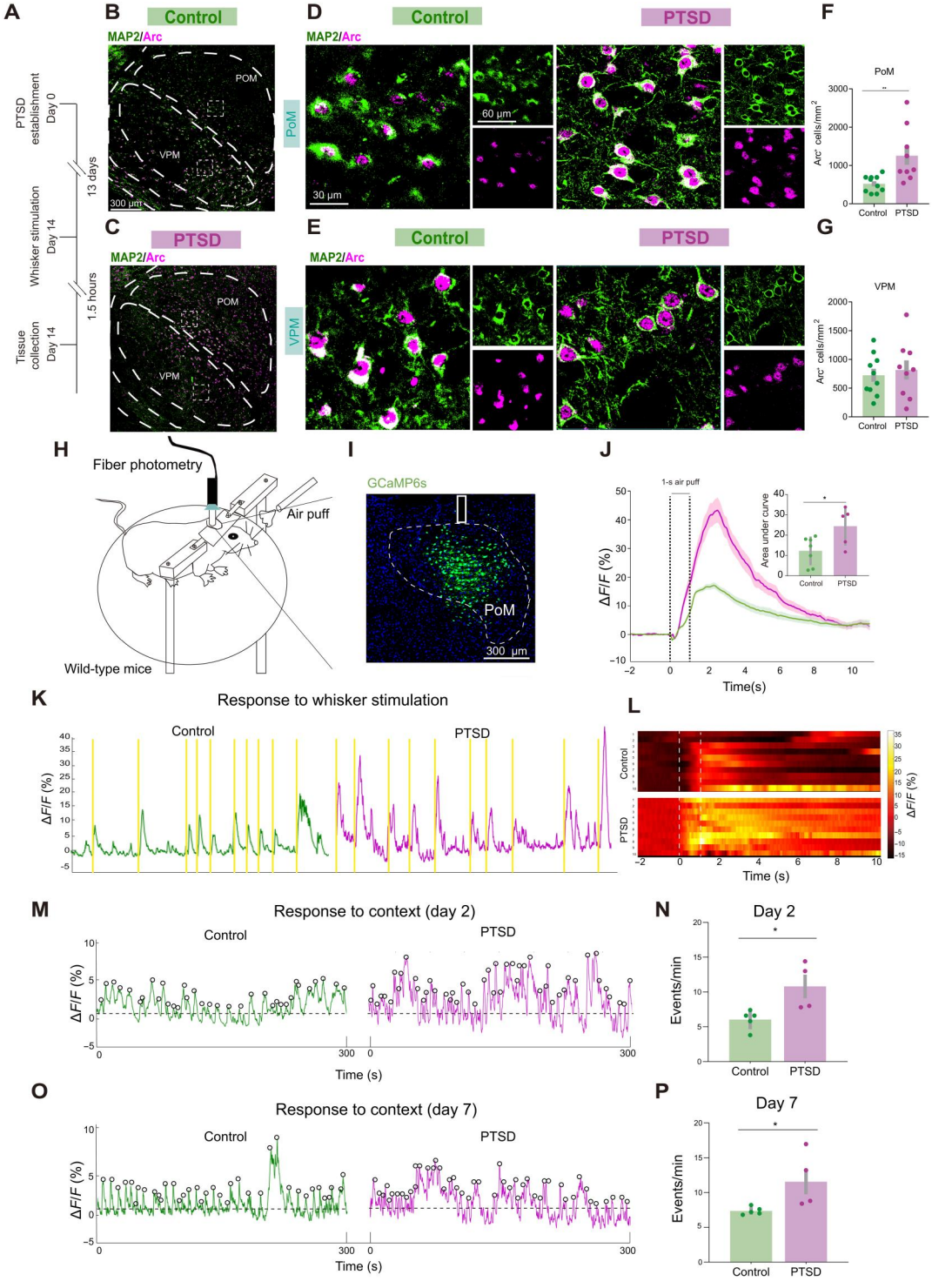

Fig. 2. PTSD mice show elevated neural activity of PoM in defensive behaviors. (**A**) Schematic of Arc and MAP2 immunofluorescence staining. (**B** to **E**) Representative images showing Arc and MAP2 expression in PoM and VPM under low magnification in control and PTSD groups. (**F**) Density of cells immunoreactive for Arc in PoM. (**G**) Density of cells immunoreactive for Arc in the VPM (n = 10 mice for the control group and n = 9 mice for the PTSD group). (**H**) Schematic of the mouse receiving air puff as whisker stimulation in fiber photometry. (**I**) Representative images showing GCaMP6 expression and fiber implanted in PoM. (**J**) Behavior-triggered average of $\Delta F/F$ signals. The latency for signal onset and the average air-puff duration plotted in bar graphs. The AUC of $\Delta F/F$ average signals in control and PTSD mice (n = 7 mice for the control group and n = 5 mice for the PTSD group). (**K**) Representative traces of GCaMP6s $\Delta F/F$ signal in control and PTSD mice, with colored rectangles indicating when the animal received whisker stimulation. (**L**) Heatmap depicting Ca^{2+} responses sorted by trial. (**M**) Representative traces of the GCaMP6 signals in control and PTSD mice when the animals entered chamber A on day 2 of the CFC test. (**N**) Frequency of calcium events in chamber A on day 2 of the CFC test (n = 4 mice for the control group and n = 5 mice for the PTSD group). (**O**) Representative traces of GCaMP6s signals in control and PTSD mice when the animals entered chamber A on day 7 of the CFC test. (**P**) Frequency of calcium events in chamber A on day 7 of the CFC test. Data are presented as means ± SEM. *P < 0.05 and **P < 0.01. See table S1 for detailed statistical information.

the number of GFP^+Arc^+ neurons in the ZI (fig. S9, B to G). The functional relevance of this observation was tested by performing patch clamp recordings in mice with TRN or ZI with the viral expression of channelrhodopsin-2 (ChR2) (Fig. 4, G and J). We recorded the inhibitory postsynaptic currents (IPSCs) with paired-pulse laser stimulation. At interpulse intervals ranging from 50 to 200 ms, the paired-pulse ratio (PPR) was increased when TRN-derived terminals were stimulated in PTSD mice (Fig. 4, H and I). However, the PPR induced by stimulation of ZI-derived terminals was intact in PTSD mice (Fig. 4, K and L). Moreover, we measured the maximal amplitude of IPSCs. We found that the amplitude of optically elicited inhibitory postsynaptic current (oIPSC) elicited by TRN-derived terminals was decreased in PTSD mice, but not that by ZI-derived terminals (fig. S10). To further explore the potential

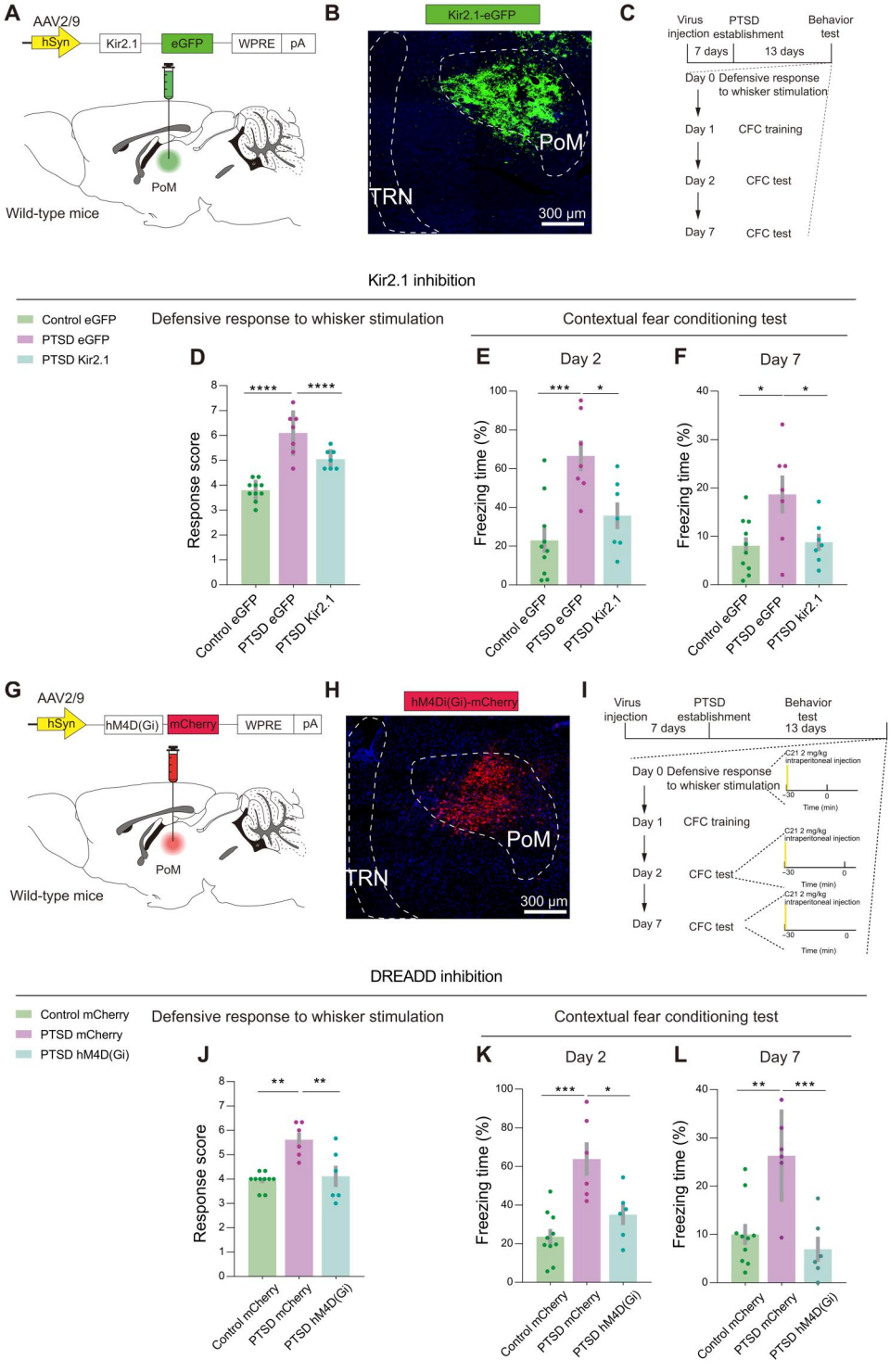

Fig. 3. PoM inhibition improves innate and learned defensive behaviors in PTSD mice. (**A**) Schematic of the viral strategy to inhibit PoM neurons through Kir2.1 overexpression. (**B**) Representative images showing Kir2.1 expression in PoM. (**C**) Schematic of the behavioral tests. (**D**) Total defensive response scores in control and PTSD mice (n = 10 mice for the control eGFP group, n = 7 mice for the PTSD eGFP group, and n = 7 mice for the PTSD Kir2.1 group). (**E**) Freezing time in the day 2 CFC test. (**F**) Freezing time in the day 7 CFC test (n = 10 mice for the control eGFP group, n = 7 mice for the PTSD eGFP group, and n = 7 mice for the PTSD Kir2.1 group). (**G**) Schematic of the viral strategy to chemogenetically inhibit PoM neurons. (**H**) Representative images showing hM4D(Gi) expression in PoM in an experimental mouse. (**I**) Schematic of behavioral tests. (**J**) Total defensive response scores in control and PTSD mice [n = 10 mice for the control mCherry group, n = 6 mice for the PTSD mCherry group, and n = 6 mice for the PTSD hM4D(Gi) mice group]. (**K**) Freezing time in the day 2 CFC test. (**L**) Freezing time in the day 7 CFC test [n = 10 mice for the control mCherry group, n = 6 mice for the PTSD mCherry group, and n = 6 mice for the PTSD hM4D(Gi) mice group]. *P < 0.05, **P < 0.01, ***P < 0.001, and ****P < 0.0001. Data are presented as means ± SEM. See table S1 for detailed statistical information.

consequences of PTSD stressors in TRN, we dissected the tissue from somatosensory part of TRN and performed bulk RNA sequencing. We found 96 up-regulated genes and 53 down-regulated genes. These genes were get involved in multiple biological processes and molecular pathways (fig. S11). Together, these data indicated that TRN was the upstream region of PoM, showing impaired inhibition in PTSD mice.

Activation of TRN-PoM circuit rescues elevated defensive responses in PTSD mice

To test the role of TRN-PoM projections in elevated defensive behaviors in PTSD mice, we first applied DREADDs to chemogenetically activate the PoM projecting TRN neurons. We bilaterally injected retrograde AAV carrying Cre in PoM and expressed hM3D(Gq) or mCherry in TRN (Fig. 5, A and B). C21 was

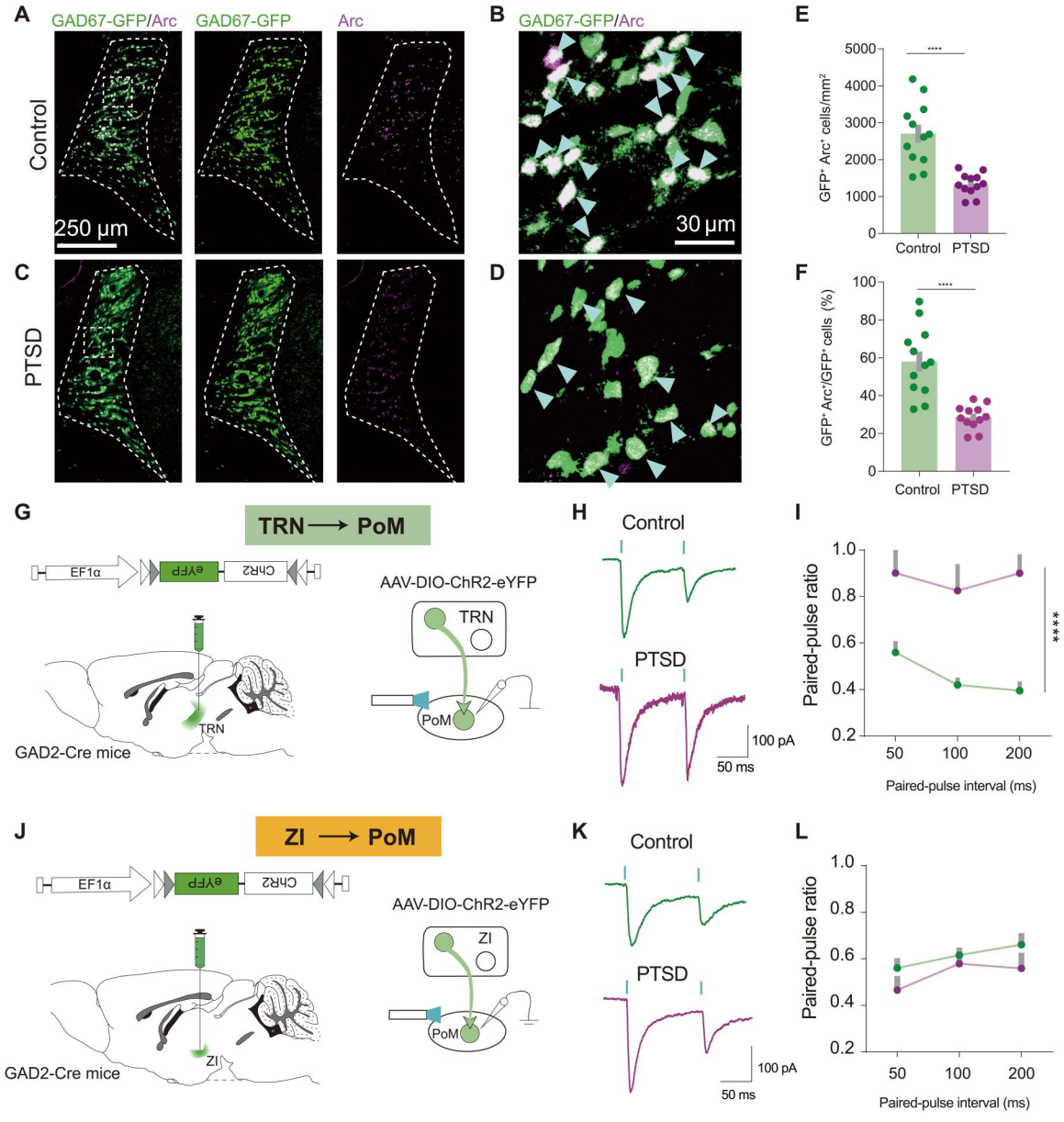

Fig. 4. Decreased TRN inhibitory inputs to PoM in PTSD mice. (**A** and **B**) Representative images showing GAD67-GFP and Arc expression in TRN in control mice. (**C** and **D**) Representative images showing GAD67-GFP and Arc expression in TRN in PTSD mice. (**E**) Density of GAD67-GFP$^+$ cells immunoreactive for Arc in TRN. (**F**) Percentage of GAD67-GFP$^+$Arc$^+$ cells in GAD67-GFP$^+$ cells in TRN (n = 12 mice for each group). (**G**) Schematic of the viral strategy for PPR recordings in PoM with photoactivation of TRN terminals. (**H**) Representative images showing the PPR of IPSC in PoM neurons with photoactivation of TRN terminals in control and PTSD mice. (**I**) Average PPR of IPSC in control and PTSD mice (n = 7 neurons for the control group and n = 8 neurons for the PTSD group). (**J**) Schematic of the viral strategy for PPR recording in PoM with photoactivation of ZI terminals. (**K**) Representative images showing PPR of IPSC in PoM neurons with photoactivation of ZI terminals. (**L**) Average PPR of IPSC in PoM neurons (n = 8 neurons for the control group and n = 7 neurons for the PTSD group). ****P < 0.0001. Data are presented as means ± SEM. See table S1 for detailed statistical information.

intraperitoneally injected into PTSD and control mice 30 min before the behavioral test to activate the PoM projecting TRN neurons (Fig. 5C). We performed Arc staining to validate the effects of DREADD activation, and we observed significantly increased expression of Arc in the hM3D(Gq) group (fig. S12). For the behavioral test, we found that C21 administration significantly attenuated excessive innate defensive responses in hM3D(Gq)-expressing PTSD mice in the total defensive response scores (Fig. 5D). Similar rescue effects of learned defensive behaviors could be observed on the 2nd day and 7th day CFC test in hM3D(Gq)-expressing PTSD mice (Fig. 5, E and F). We validated the virus injection sites after behavioral tests (fig. S13A).

To further manipulate this projection with better circuitry specificity, we bilaterally expressed the stable step-function opsin (SSFO) in the TRN with PV-Cre mice and planted fibers upon the PoM (Fig. 5, G and H, and fig. S14). SSFO could maintain

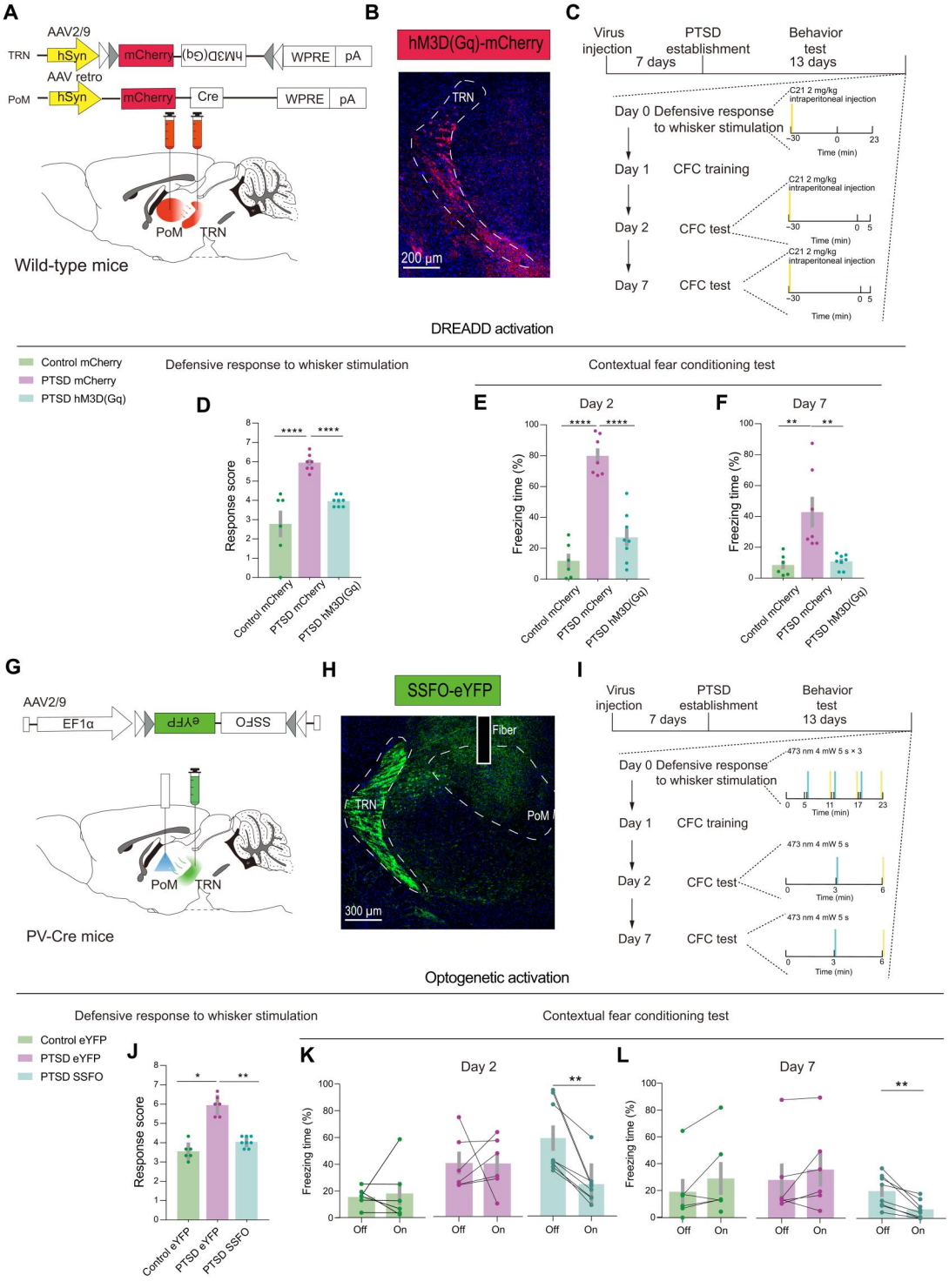

Fig. 5. Activation of TRN-PoM circuit improves excessive innate and learned defensive behaviors in PTSD mice. (**A**) Schematic of the viral strategy to chemogenetically activate TRN neurons projecting to PoM. (**B**) Representative images showing hM3D(Gq) expression in TRN. (**C**) Schematic of behavioral tests. (**D**) Total defensive response scores in control and PTSD mice [$n = 6$ mice for the control mCherry group, $n = 7$ mice for the PTSD mCherry group, and $n = 8$ mice for the PTSD hM3D(Gq) group]. (**E**) Freezing time in the day 2 CFC test. (**F**) Freezing time in the day 7 CFC test [$n = 6$ mice for the control mCherry group, $n = 7$ mice for the PTSD mCherry group, and $n = 8$ mice for the PTSD hM3D(Gq) group]. (**G**) Schematic of the viral strategy to optically activate axons of TRN projecting to PoM. (**H**) Representative images showing SSFO expression in TRN and optical fiber site in PoM. (**I**) Schematic of behavioral tests. (**J**) Response scores of total defensive responses in control and PTSD mice ($n = 6$ mice for the control eYFP group, $n = 6$ mice for the PTSD eYFP group, and $n = 8$ mice for the PTSD SSFO group). (**K**) Freezing time in the day 2 CFC test. (**L**) Freezing time in the day 7 CFC test ($n = 6$ mice for the control eYFP group, $n = 6$ mice for the PTSD eYFP group, and $n = 8$ mice for the PTSD SSFO group). Data are presented as means ± SEM. $^*P < 0.05$, $^{**}P < 0.01$, and $^{****}P < 0.0001$. See table S1 for detailed statistical information.

remarkable stability of the activated states for a time scale of over 30 min after receiving a 473-nm light and could be blocked by a 560-nm light (*22*). We tested the effects of SSFO with slice recordings and found that with 473-nm light illuminating, the PoM cells would show increased IPSCs and the 560-nm light would turn off this effect (fig. S15). All mice received a 5-s 473-nm light through the implanted fiber before the behavior tests (Fig. 5I). As expected, optogenetic activation of TRN axons in the PoM significantly reduced excessive innate defensive behaviors in response to whisker stimuli in the total response score (Fig. 5J). Compared with both enhanced yellow fluorescent protein (eYFP)–expressing PTSD groups, SSFO-expressing PTSD mice exhibited a significant decrease after optogenetic activation of TRN axons in the PoM on the 2nd and 7th day CFC test (Fig. 5, K and L). We validated the

virus injection sites after behavioral tests (fig. S13B). Thus, enhancing the inhibition from TRN to PoM could effectively improve the excessive defensive behaviors in PTSD mice.

FrA downstream of PoM mediates excessive defensive behaviors in PTSD mice

We used the TRAP strategy combined with the anterograde tracing to examine the downstream cortical regions of PoM mediating defensive behaviors. Fos-TRAP could precisely express Cre on the neurons, which is activated by specific stimuli in the time window of tamoxifen injection (*23*). We first unilaterally injected AAV-DIO-eGFP in the PoM in Fos-CreER^{T2} mice. Tamoxifen (100 mg/kg) was intraperitoneally injected into the mice 23 hours before whisker stimulation for 5 min in three consecutive days (Fig. 6A). We observed dense eGFP-expressing neurons in the PoM. For the cortical regions, the FrA showed robust eGFP signals (Fig. 6, B to D, and fig. S16).

Limited studies have reported the connectivity between the PoM and FrA. We applied two retrograde tracing strategies to confirm the anatomical connection. First, we unilaterally injected a non–downstream-defined tracer, retrobeads, into FrA and found a large number of beads in the PoM (Fig. 6, E to I). Second, we conducted monosynaptic retrograde tracing using the rabies virus strategy. By injecting the CaMKII-Cre virus in FrA combined with Cre-dependent AAV helper targeting the pyramidal neurons, we characterized the PoM-innervated FrA pyramidal neurons with high specificity (Fig. 6, J to N). The functional connectivity was tested by using in vitro electrophysiology to record the excitatory postsynaptic current (EPSC) of FrA neurons evoked by photoactivation of the PoM axons. EPSCs in FrA neurons were recorded followed by a 2-ms blue laser in the mice injected with CaMKII-Cre and DIO-ChR2-eYFP into the PoM (Fig. 6O). The EPSCs could be fully blocked by 6-Cyano-7-nitroquinoxaline-2,3-dione (CNQX), a potent and competitive AMPA/kainate receptor antagonist (Fig. 6, P and Q). These results suggested a strong connection of PoM with the downstream FrA, and the projection was glutamatergic.

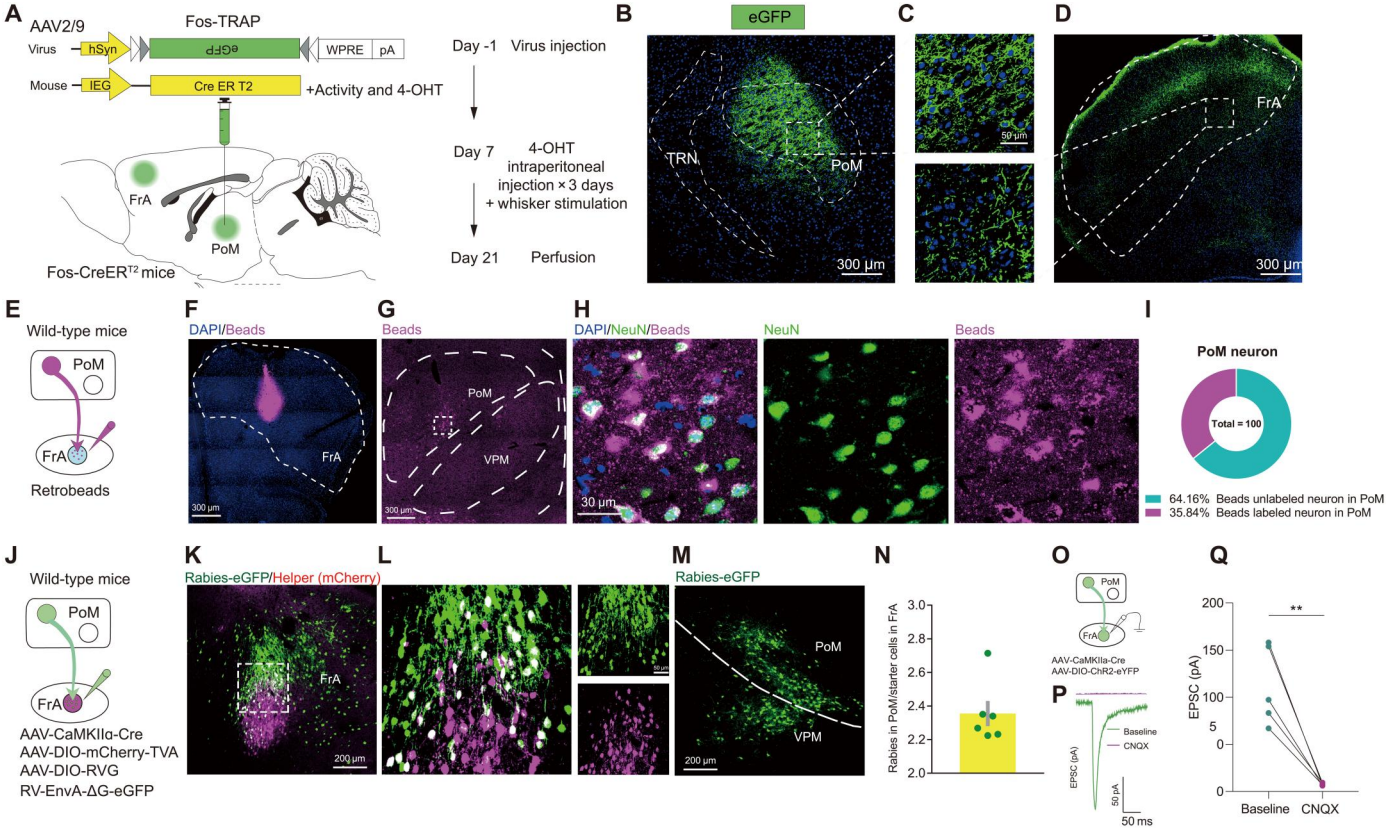

Fig. 6. PoM-FrA projection is monosynaptic and functionally related to defensive behaviors. (**A**) Schematic of Fos-TRAP strategy for anterograde tracing of the downstream regions of PoM. (**B** to **D**) Representative images showing eGFP expression in PoM and FrA. (**E**) Schematic of retrobead injection for retrograde tracing of upstream regions of FrA. (**F**) Representative images showing retrobead expression in FrA under low magnification. (**G**) Representative images showing retrobead expression in PoM under low magnification. (**H**) Representative images showing retrobead expression and NeuN staining in PoM. (**I**) Pie chart of the percentage of retrobead$^+$ neurons in PoM neurons. (**J**) Schematic of rabies virus injection for retrograde tracing of the upstream regions of FrA. (**K**) Representative images showing starter cell expression in FrA under low magnification (left). (**L**) Representative images showing starter cell expression in FrA under high magnification. (**M**) Representative images showing rabies expression in PoM under low magnification. (**N**) Histogram for numbers of rabies-labeled PoM neurons normalized to the number of starter cells. (**O**) Schematic of viral strategy for EPSC recording in FrA evoked by PoM. (**P**) Representative images showing EPSC of neurons in FrA evoked by PoM inputs with (purple) and without (green) CNQX infusion. (**Q**) EPSC of neurons in FrA evoked by PoM inputs with (purple) and without (green) CNQX infusion ($n = 5$ neurons from three mice). Data are presented as means ± SEM. $^{**}P < 0.01$. See table S1 for detailed statistical information.

A previous study has reported that the synaptic plasticity of FrA neurons was relevant for associated learning and that the morphological changes correlate with the postsynaptic strength of synapses (*24*). Therefore, we explored whether FrA would show plasticity changes following long-term overload of thalamic inputs in PTSD mice. We introduced the dual eGFP reconstitution across synaptic partners (dual-eGRASP), enabling selective labeling of synapses in FrA originating from specific neuronal populations of the PoM (fig. S17, A to C). Dual-eGRASP is an intensified split fluorescent protein that can only emit fluorescence when pre- and postsynaptic GRASP components are physically attached to the synaptic cleft (fig. S17, D to G) (*25*). We examined parameters corresponding to spine morphology at PoM-FrA synapses and found a significant increase in the spine volume and spine head volume in the PoM-FrA pathway (fig. S17, H to J).

We bilaterally expressed a light-activated chloride pumping halorhodopsin, eNpHR 3.0, into PoM and planted two optical fibers into the FrA to directly test the role of the PoM-FrA pathway in defensive behaviors (Fig. 7, A to C). After delivering constant stimulation of the 560-nm light, the eNpHR-expressing PTSD mice exhibited significantly decreased total response scores (Fig. 7D). The 560-nm light stimulation did not affect the eYFP-expressing PTSD mice and eYFP-expressing control mice (Fig. 7D). Moreover, eNpHR-expressing PTSD mice exhibited significantly decreased freezing time when exposed to a traumatic environment with optogenetic inhibition, which could not be observed in eYFP-expressing PTSD mice and control mice (Fig. 7, E and F). The injection sites were validated (fig. S18). Together, these results demonstrated that inhibiting the PoM-FrA pathway could reduce defensive behaviors in PTSD mice and that the FrA was downstream of PoM, regulating the defensiveness.

DISCUSSION

Defensive behaviors in PTSD mouse models

Previous studies have demonstrated that patients with PTSD exhibit dysregulation of normal fear processes (*26*), exaggerated response to trauma-related triggers (*27*), and abnormal fear learning (*28*), which are quintessentially defensive behaviors because they develop in reaction to outward threats. For translational research on PTSD, many animal models have been established. As one of the leading animal models used in PTSD research, the fear conditioning (FC) model is widely applied due to its remarkable resemblance to conditioned fear behavior. However, this model is also criticized for lacking clear relevance to non–fear-related symptoms (*29*). The psychosocial predator-based mouse model, introducing predator exposure and social instability as stressors, was widely applied as an effective PTSD model for its increased anxiety and

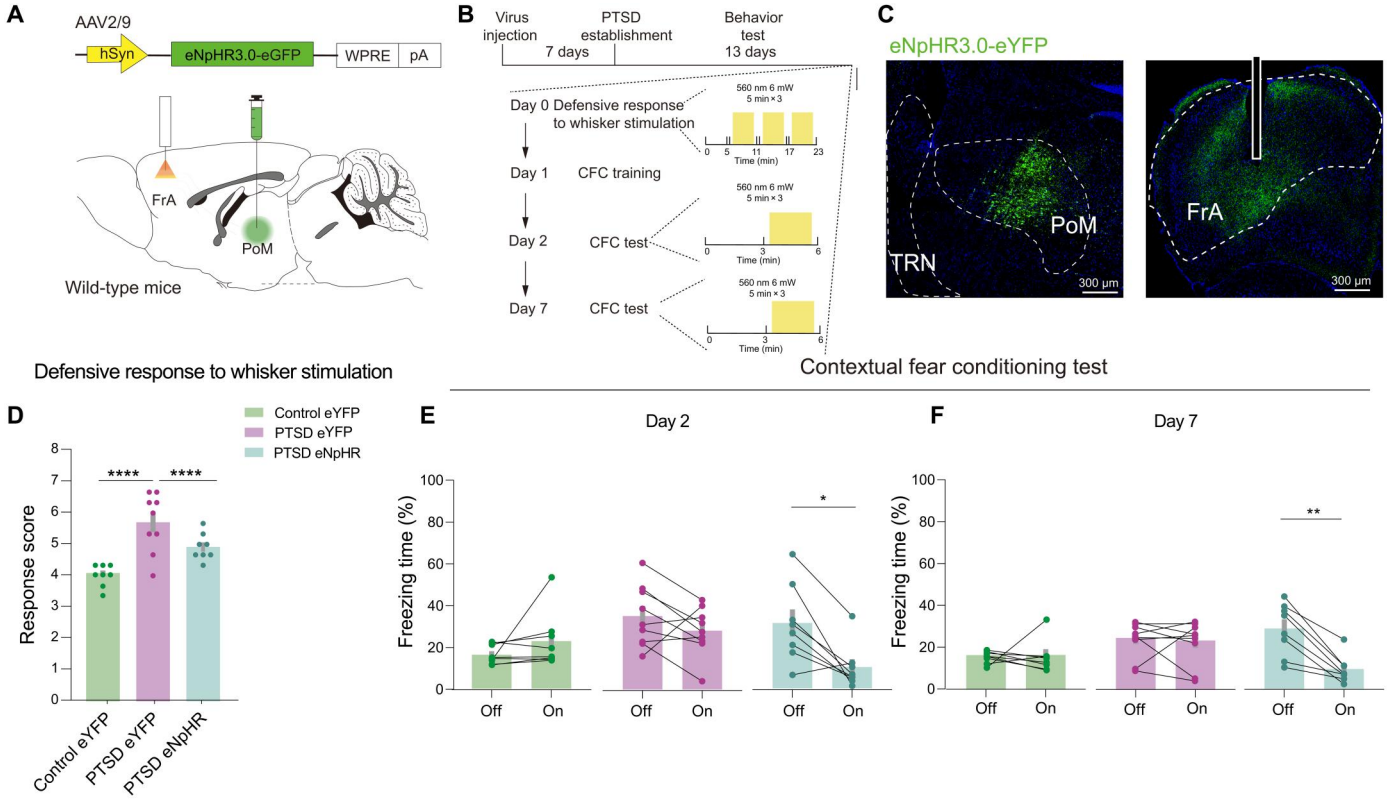

Fig. 7. Inhibition of PoM-FrA circuit rescues excessive innate and learned defensive behaviors in PTSD mice. (**A**) Schematic of the viral strategy to optically inhibit axons of PoM projecting to FrA. (**B**) Schematic of behavioral tests. (**C**) Representative images showing eNpHR expression in PoM and the optical fiber site in FrA in an experimental mouse. (**D**) Total defensive response scores in control and PTSD mice ($n = 8$ mice for the control eYFP group, $n = 9$ mice for the PTSD eYFP group, and $n = 8$ mice for the PTSD eNpHR group). (**E**) Freezing time in the day 2 CFC test. (**F**) Freezing time in the day 7 CFC test ($n = 8$ mice for the control eYFP group, $n = 9$ mice for the PTSD eYFP group, and $n = 8$ mice for the PTSD eNpHR group). Data are presented as means ± SEM. $^*P < 0.05$, $^{**}P < 0.01$, and $^{****}P < 0.0001$. See table S1 for detailed statistical information.

impaired object recognition memory (*30*). Furthermore, genetically modified animals have also been used in mechanistic studies of PTSD. For instance, Pet-1 knockout mice could mimic the anxiety- and depression-related behaviors, reflecting reactivity to threat in PTSD patients (*31*). A modified SPS model was used in our previous study of the therapeutic investigation of PTSD for analyzing the abnormalities of emotion-related and threat-derived behaviors in PTSD (*32*). We also previously integrated the SPS model with an SPS&S FC and elucidated that the model could effectively recapitulate neural and electroencephalography profiles in PTSD patients. The SPS&S mouse model exhibited excessive innate defensive behaviors for tactile threats and learned defensive behaviors for trauma-related environmental stimuli (*17*). Therefore, this model is suitable for translational preclinical investigations of PTSD defensive behaviors.

Role of HO thalamus in PTSD

On the basis of different functions and input sources, the thalamus is divided into the first-order nucleus receiving subcortical sources and the HO relay nuclei driven by input from layer 5 of the cortex that participates in the cortico-thalamocortical (TC) (or transthalamic) circuit (*33*). It has been reported that the HO thalamus is involved in sensory-related cognitive function (*34*) and attention (*35*), and the defects in these functions have been observed in PTSD patients (*1*). Over the past two decades, accumulating evidence from clinical studies has identified thalamic abnormalities in PTSD. A functional magnetic resonance imaging investigation using the script-driven symptom provocation paradigm has shown a lower activation level in the thalamus in subjects with PTSD in all three emotional states (sad, anxious, and traumatic) (*36*). However, another study detected increased activity in certain parts of the HO thalamus, such as the anterior and mediodorsal thalamus in PTSD during implicit trauma-related trigger processing with threatening pictures (*37*), consistent with our findings of HO thalamus hyperactivity. The heterogeneity of PTSD, distinct behavioral paradigms, and different observation parameters may contribute to these contradictory results. Moreover, we found that the PoM displayed increased activity while receiving tactile or environmental stimuli, consistent with its physiological function as the HO somatosensory thalamus (*38*). Because the HO thalamus could respond to diverse stimuli, the hyperactivation of differential thalamic regions in PTSD could be observed under specific circumstances. Further study should be carried out to characterize the changes of other HO thalamus and explore the roles in the behavioral abnormalities of PTSD.

Regulation of defensive behaviors by HO thalamus

Multiple brain regions have been implicated in driving defensive behaviors (*39*). Amygdala has been reported to participate in learned defensive behaviors (*40*). Notably, different regions of the amygdala have various roles in defensive behaviors. The central nucleus of the amygdala (CeA) encodes freezing and flight behaviors by innervating the ventrolateral periaqueductal gray (*41*). In contrast, the neuronal population of the basolateral amygdala (BLA) participates in fear extinction behaviors (*42*). Besides the amygdala, ventral tegmental area (VTA) glutamatergic neurons regulated by the lateral hypothalamic area are activated and required for innate defensive responses or escape responses (*43*). Besides, VTA^{GABA+} neurons respond to a looming stimulus by projecting to CeA (*44*) and activating GABAergic neurons in the dorsal raphe nucleus participate in translating visual threats into defensive behavioral responses (*45*). Different from the regions above, the HO thalamus is a gateway integrating information from multiple cortical areas and has been reported to contribute to defensive behaviors (*8*). HO auditory thalamus medial geniculate correlates with memory-related defense through $GABA_BR$-mediated presynaptic modulation (*8*). However, the role of the HO somatosensory thalamus in PTSD mice has not been elucidated. In the present study, we found that the PoM showed hyperactivation when confronting tactile or environmental threats, but not auditory stimulation. Chemogenetic inhibition of PoM could diminish excessive defensive behaviors. For rodents, tactile information is one of the essential external factors while exploring the environment. PoM is the HO thalamic region that receives whisker-associated tactile information, but not auditory information (*46*), which makes sense for the data related to contextual-induced responses. However, how the PoM processes the information and encodes the defensive behaviors still needs to be clarified.

Regulation of defensive behaviors by thalamic inhibition

Abnormal thalamic inhibition has been recognized as one of the key pathological alterations in many psychiatric disorders, including ASD, ADHD, and SCZ (*15*, *47*, *48*). Altered inhibitory inputs to TC circuits, caused by gene mutations or environmental stresses, would lead to an array of behavioral abnormalities related to cognition (*49*). The role of thalamic inhibition has also been implicated in modulating defensive behaviors, the abnormalities of which are common in psychiatric disorders (*16*). From the anatomical perspective, the inhibitory axons within the thalamus are mainly derived from TRN and specific extrathalamic inhibitory system, such as ZI (*33*). Distinct TRN subregions could generate diverse behavioral responses to environmental threats. Limbic TRN mediates flight (*16*), while rostroventral TRN is required for auditory system–derived fear extinction (*50*). Besides reticular inhibition, ZI inhibition has also been reported to be relevant to innate and learned defensive behaviors (*51*). Intriguingly, a previous study has also suggested that the enhanced PoM projecting neurons in ZI contributed to defensiveness (*52*), consistent with our notion that PoM serves a critical role in mediating behavioral responses to threats. Although these findings strongly suggested that thalamic inhibition is vital for neural encoding of defensive behaviors, there is limited experimental evidence and the possible role of thalamic inhibition in the occurrence of PTSD symptoms has not been investigated. In our study, we used optogenetic-based approaches to characterize the sources of thalamic inhibition and found that reticular inhibition, but not ZI inhibition, causes thalamic hyperactivity in the PTSD mouse model, resulting in excessive defensiveness.

HO-involved TC regulation in defensive behaviors

HO thalamic nuclei play an essential role in cortical function by connecting cortical and subcortical brain regions (*53*). Alterations of the HO-TC circuit due to cortical oscillation interference and pathological synaptic interactions might provoke dysregulation of HO behaviors, including learning, attention, and cognitive function (*54*–*56*). In addition, TC regulation is essential in the management of mammalian defense behaviors, affecting the daily lives of patients diagnosed with psychopathologies (*57*). However, current studies of the HO-TC circuit focus on predicting threats instead of defensive

behaviors. The interactions between the lateral posterior nucleus of the thalamus and the primary visual cortex (V1) contribute to feature selectivity and filtering of unwanted threat-related information (*55*). However, there are limited studies on TC regulation of defensive behaviors in PTSD. PoM has been reported to be involved in defensive behaviors (*52*) and could provoke sensory enhancement through monosynaptic excitation and disinhibition of neurons in primary and secondary somatosensory cortices, the motor cortex, and association cortices (*56*), which are considered as regions subserving executive, socioemotional, and mentalizing functions (*58*). As one of the association cortices, the FrA is involved in drug addiction (*59*), fear response, aggressiveness, and social interactions (*24*). In this study, we first defined that the PoM-FrA pathway participates in innate and learned defensive behaviors in response to outward threats by the Fos-TRAP strategy (*23*) and optogenetic regulation. We observed notable changes in synaptic plasticity of PoM-derived FrA dendritic spines in PTSD. Previous studies have found that FrA integrates fear response by receiving inputs from BLA in an N-methyl-D-aspartate (NMDA) receptor-dependent manner (*24*). Therefore, we hypothesized that synaptic plasticity changes in FrA might result from the rapid exchange of neurotransmitter receptors between synapses of PoM and FrA in PTSD, which deserves further exploration. In addition, the morphology of spines in the FrA has been reported to be relevant to circuit strengthening and regulating defensive behaviors (*60*). In this study, we used the dual-eGRASP technique to investigate the dynamic changes of spines in a particular circuit, under PTSD conditions. We provided morphological evidence of synaptic strengthening on a TC circuit, which may result from the hyperactivity of HO thalamus in an activity-dependent manner. Together, our findings illustrate that HO thalamus PoM is a core in regulating innate and learned defensive behaviors for outward threats in PTSD. Thalamic inhibition contributes to the dysregulation of defensive behaviors in PTSD. In addition, the reversal of the overactivated PoM-FrA circuit could rescue excessive defensive behaviors in PTSD, which highlights a potential therapeutic target for PTSD patients with important translational significance.

MATERIALS AND METHODS

Animals

C57BL/6J wild-type male mice were obtained from Beijing Vital River Laboratory. GAD2-Cre mice (stock no. 028867, The Jackson Laboratory) and PV-Cre mice (stock no. 017320, The Jackson Laboratory) consisted of the GAD2-IRES-Cre and B6 PV-Cre knock-in lines, respectively. GAD67-GFP mice were a gift from N. Tamamaki (Kumamoto University) (*61*). The c-fos-CreER^{T2} mouse line (*23*) was obtained from Shanghai Model Organisms (stock no. NM-KI-200110) for TRAP experiments.

Mice were housed in a room maintained at a constant temperature on a 12-hour light/dark cycle (light from 08:00 to 20:00). All transgenic and knock-in mouse lines were maintained as hemizygotes. Mice had access to food and water ad libitum and were socially housed in numbers of two to five littermates randomly until surgery. Following surgery, mice were housed undisturbed. All mice were male and 3 to 5 months old for behavioral experiments. All procedures were approved by the Institutional Animal Care and Use Committee of the Fourth Military Medical University following Animal Research: Reporting of In Vivo Experiments (ARRIVE) guidelines (FMMULL-220926) and conformed to the *Guide for the Care and Use of Laboratory Animals* published by the National Institutes of Health. Animals were randomized to different treatments according to a group of pregenerated random numbers by Excel.

PTSD establishment (SPS&S stress)

We used four stressors in this study: restraint stress, forced swim, deep anesthesia, and unconditioned foot shock. The mouse fetter was used to constrain the experimental group of mice for 4 hours in their home cage, following which mice were left free in a big cage (50 cm × 40 cm × 30 cm) to rest for 30 min. Subsequently, the mice were forced to swim for 20 min in a plastic tub (20 cm diameter, 30 cm height) filled with water (25°C) with a waterline of 20 cm. Then, they were left in their home cage to recuperate for 30 min. The mice were then exposed to ether and anesthetized until the characteristics of rapid breathing and loss of responses to toe and tail pinch were evident. After a 30-min interval, an unconditioned foot shock (0.8 mA, 5 s) was applied to the experimental group in a chamber (20 cm × 20 cm × 20 cm) with an electrical grid floor to provide foot shock. The group of control mice was also placed in the same chamber for 5 s to experience the environmental stimulus. The mice were then returned to their home cage and left undisturbed.

Viruses

AAV-hSyn-eGFP [serotype 2/9, titer 1.12×10^{13} vector genome per ml (vg/ml)], AAV-hSyn-mCherry (serotype 2/9, titer 5.04×10^{12} vg/ml), AAV-DIO-ChR2(H134R)-eYFP (serotype 2/9, titer 5.04×10^{12} vg/ml), AAV-hSyn-DIO-hM3D(Gq)-mCherry (serotype 2/9, titer 2.90×10^{12} vg/ml), and AAV–hSyn–eNpHR 3.0–eYFP (serotype 2/9, titer 1.45×10^{12} vg/ml) were purchased from Brain VTA, Wuhan. AAV-hSyn-GCaMP6s (serotype 2/9, titer 2.60×10^{12} vg/ml), AAV-hSyn-hM4D(Gi)-mCherry (serotype 2/9, titer 2.23×10^{12} vg/ml), AAV-EF1a-DIO-hChR2(H134R)-eYFP (serotype 2/9, titer 3.20×10^{12} vg/ml), RV-EnvA-$^{\Delta}$G-eGFP (serotype 1, 1.50×10^{8} IFU/ml), AAV-hSyn-DIO-mCherry (serotype 2/9, titer 4.60×10^{12} vg/ml), AAV-nEF1α-DIO-NLS-mCherry-F2A-TVA-T2A-RVG (serotype 2/9, titer 2.40×10^{12} vg/ml), AAV-EF1α-DIO-oRVG(19G) (serotype 2/9, titer 2.05×10^{12} vg/ml), and AAV-CaMKIIα-Cre (serotype 2/9, titer 2.51×10^{12} vg/ml) were purchased from Brain Case, Shenzhen. AAV-hSyn-Kir2.1 (serotype 2/9, titer 2.19×10^{12} vg/ml), AAV-CAG-pre-mGRASP-mCerulean (serotype 2/9, titer 1.0×10^{13} vg/ml), and AAV-CAG-post-mGRASP-2A-dTomato (serotype 2/9, titer 1.0×10^{13} vg/ml) were purchased from Taitool Bioscience Co., Shanghai. AAV2/retro-pAAV-hSyn-mCherry-Cre (serotype 2/9, titer 5.40×10^{12} vg/ml) and AAV-DIO-eGFP (serotype 2/1, titer 1.03×10^{13} vg/ml) were purchased from Obio Technology Co., Shanghai.

Mouse surgery and optic fiber implantation

Animals were anesthetized with isoflurane for stereotaxic injections and were given meloxicam (1 mg kg^{-1}) as an analgesic before incisions. Injections were targeted to PoM [−1.82 mm anterior-posterior (AP), ±1.10 mm medial-lateral (ML), −3.10 mm dorsal-ventral (DV)], TRN (−1.82 mm AP, ±2.20 mm ML, −3.25 mm DV), and FrA (+2.60 mm AP, ±1.50 mm ML, −1.50 mm DV). Standard injection volumes were 250 nl for PoM and TRN and were used for all experiments except for certain retrograde tracing experiments with rabies virus. In the rabies virus (RV) tracing experiment, the virus

injection for AAV helper and CaMKIIα-Cre mixture was 400 nl and RV ($^{\Delta}$G) was 100 nl for each mouse. The needle was lowered to the target site and remained for 5 min before infusion. After the injection, the needle stayed for 10 min before it was withdrawn. For behavioral manipulation experiments using optogenetics, the single monofiber implant (core diameter, 200 mm; Braincase) was higher either above injection sites or terminals bilaterally PoM (−1.82 mm AP, ±1.10 mm ML, −2.90 mm DV) and FrA (+2.60 mm AP, ±1.50 mm ML, −1.30 mm DV). The implant was secured to the skull with dental cement. Mice were given sustained-release buprenorphine (1 mg/kg) as an analgesic after the surgery. Mice were allowed to recover for at least 2 weeks before behavioral experiments. All injection sites were verified histologically. We only included mice with virus expression limited to the targeted regions.

Fiber photometry recordings

Fiber photometry recordings were carried out as previously described (*62*, *63*). Briefly, animals were single housed for 1 week before recording. Before each recording session, the implanted optic fiber was connected through an external optical fiber to the recording setup (Thinker Tech, Nanjing). To excite GCaMP6s, a 473-nm light-emitting diode (LED) (Cree XP-E LED) was reflected off a dichroic mirror (MD498, Thorlabs) that was focused using a 0.4 numerical aperture (NA) 20× objective lens (Olympus) and coupled to an optical commutator (Doris Lenses). An optical fiber (230 μm optical density, 0.37 NA) guided the light between the commutator and the implanted optical fiber. The laser power at the tip of the optical fiber was adjusted to 0.01 to 0.02 mW to decrease laser bleaching. Fluorescence was bandpass-filtered (MF525-39, Thorlabs), and an amplifier was used to convert the CMOS (complementary metal-oxide semiconductor) (DCC3240M, Thorlabs) current output to signals, which were further filtered through a low-pass filter (40-Hz cutoff, ThinkerTech). The analog voltage signals were digitalized at 50 Hz and recorded by the multichannel fiber photometry recording system (ThinkerTech). Before the introduction of the stimuli, animals were allowed to habituate on the air float where the mouse could freely move on the floor for 10 min, during which time baseline fluorescent signals were collected. For comparison of responses to air-puff stimulation in Fig. 2 and fig. S3, only one recording session was performed each day, in which air puffs were presented in a balanced manner, each with a break until the mouse calmed down. Fluorescence signals were recorded continuously during the entire trial of air-puff stimulation and normalized ($\Delta F/F$ median signal. For event frequency analysis, data exceeding 2.91 times the median absolute deviation (MAD) of baseline and remaining above 2 times MAD of baseline were considered a calcium signal event. In a recording cycle, the number of events divided by the time is the event frequency. The heatmap and averaged Ca^{2+} traces were plotted using a self-developed MATLAB program.

Immunohistochemistry

Histological analysis was performed as previously described (*17*). Mice were anesthetized using an overdose of isoflurane and transcardially perfused with 50 ml of 0.01 M phosphate-buffered saline (PBS) (pH 7.4) followed by 50 ml of 4% paraformaldehyde in 0.2 M phosphate buffer (pH 7.4). Brains were rapidly removed and fixed for 4 hours at 4°C. After dehydrating twice with 30% sucrose solution for 48 hours at 4°C, brain sections (50 μm) were sliced on a freezing microtome (CM1950, Leica, Germany). The brain regions included PoM, FrA, and TRN. The sections from each group (three to six sections per region) were rinsed in PBS + 0.2% Triton X-100 (PBS-T), with 5% normal goat serum for 2 hours followed by incubation with primary antibodies overnight at 4°C. Sections were then washed three times with PBS and probed with secondary antibodies for 4 hours. After three more washing steps of 10 min each in PBS, the slices were incubated with 4′,6-diamidino-2-phenylindole (DAPI) for nuclear staining for 15 min. Last, the slices were washed three more times with PBS and mounted on microscope slides. Sections were observed with a confocal microscope (FV3000, Olympus, Japan) and 10× objective fluorescent microscope (VS200, Olympus, Japan). Antibodies used for staining were as follows: primary antibodies: rabbit anti-Arc antibody (1:3000, Synaptic Systems), rabbit anti-NeuN (1:1000, Sigma-Aldrich), and mouse anti-MAP2 (1:1500, Sigma-Aldrich) and the corresponding fluorescence secondary antibodies: goat anti-rabbit Alexa Fluor 488 (1:500, Invitrogen), goat anti-mouse Alexa Fluor 594 (1:500, Invitrogen), goat anti-rabbit Alexa Fluor 647 (1:500, Jackson ImmunoResearch), and DAPI (1:1000, Sigma-Aldrich). Details of antibodies were listed in table S3. For Arc-related cell counting, we used GAD67-GFP to visualize the TRN and used the shape of TRN as a landmark to identify PoM and VPM. For spine analysis, we collected 10 slices from three control mice and 11 slices from three PTSD mice. Morphological analysis was performed by Imaris software (v.9.5.0, Bitplane, Switzerland). Each mGRASP-positive dendrite was manually marked as a filament. Each pre-mGRASP-mCerulean signal projected from PoM was marked as a spot through automatic detection. Dendrites in the FrA without any mGRASP overlapping were excluded from more precise analysis. Spines of designated eGRASP- and mGRASP-positive dendrites were manually reconstructed with automatic detection of diameter and volume. Spine head max diameter, spine head volume, and spine volume were measured with Imaris Filament. Normalization of the raw data was done within each dendrite. All analyses were performed in a blinded fashion to the experimental conditions.

Fos-TRAP labeling

Animals were anesthetized with isoflurane for stereotaxic injections with meloxicam (1 mg kg^{-1}) as an analgesic before incisions. Injections were targeted to PoM (−1.82 mm AP, +1.10 mm ML, −3.10 mm DV). AAV-DIO-eGFP (500 nl) was injected into PoM unilaterally per mouse for a week before stimulation. As mentioned above, Fos-CreER^{T2} mice were used for activity-dependent labeling experiments. Tamoxifen (Sigma-Aldrich) was dissolved at 20 mg/ml in corn oil (Sigma-Aldrich, catalog no. C8267) by rotation at room temperature for 4 to 8 hours. Tamoxifen (20 mg/ml) was stored for a maximum of 24 hours at 4°C before use. All injections were delivered intraperitoneally. For each mouse, optimal activity-dependent labeling was achieved using a target concentration of 100 to 150 mg/kg. Mice were injected with tamoxifen 23 hours before the behavioral epoch of interest. Following whisker stimulation, mice remained undisturbed for 2 weeks until they were perfused for histological analyses.

Chemogenetic and optogenetic experiments

For chemogenetic [i.e., hM4D(Gi) or hM3D(Gq)] neuronal activity manipulation experiments, we used the second-generation agonist known as C21 (Tocris). This agonist in dihydrochloride form was dissolved in sterile saline at 10 mg/ml and kept as frozen aliquots. For each mouse, optimal chemogenetic activity was achieved using a target concentration of 2 mg/kg (injected intraperitoneally) 30 min before the behavioral epoch of interest. For optogenetic neuronal activity manipulation experiments, SSFO was activated with a 473-nm laser (4 mW, blue light) for 5 s and blocked with a 560-nm laser (10 mW, green light) for 5 s. eNpHR 3.0 was activated with a 560-nm laser (10 mW, constant green light).

Slice electrophysiological recording

As described previously, a whole-cell patch-clamp recording was performed (*62*). Briefly, 3 weeks after viral injection of AAV-ChR2 into the bilateral TRN or ZI, mice were anesthetized with isoflurane and transcardially perfused with ice-cold carbogenated (95% O_2, 5% CO_2) cutting solution containing the following: 115 mM choline chloride, 2.5 mM KCl, 1.25 mM NaH_2PO_4, 0.5 mM $CaCl_2$, 8 mM $MgCl_2$, 26 mM $NaHCO_3$, 10 mM D-(+)-glucose, 0.1 mM L-ascorbic acid, and 0.4 mM sodium pyruvate (300 to 305 mOsm liter^{-1}). Coronal slices (330 μm thick) containing the PoM (bregma, −1.34 to −2.54 mm, determined by the shapes of lateral ventricles and hippocampus) were prepared using a vibratome (VT1200S, Leica). Whole-cell patch-clamp recordings were performed using infrared differential interference contrast visualization at 28° to 30°C in artificial cerebral spinal fluid containing the following: 119 mM NaCl, 2.3 mM KCl, 1.0 mM NaH_2PO_4, 26 mM $NaHCO_3$, 11 mM D-(+)-glucose, 1.3 mM $MgSO_4$, and 2.5 mM $CaCl_2$ (pH 7.4, 295 to 300 mOsm liter^{-1}). Patch pipettes were filled with a solution containing the following for IPSC recordings: 103 mM CsCl, 12 mM CsOH, 12 mM methanesulfonic acid, 10 mM Hepes, 4 mM NaCl, 5 mM tetraethylammonium chloride (TEA-Cl), 0.5 mM EGTA, 10 mM phosphocreatine, 4 mM Na_2ATP, 0.3 mM Na_2GTP, and 5 mM QX-314 (pH 7.3, 300 to 305 mOsm liter^{-1}). For EPSCs, pipettes were backfilled with the internal solution containing 120 mM $CsMeSO_3$, 5 mM NaCl, 10 mM TEA-Cl, 10 mM Hepes, 5 mM TEA-Cl, 1.1 mM EGTA, 10 mM phosphocreatine, 4 mM MgATP, 0.3 mM Na_2GTP, and 4 mM QX-314. The recordings were obtained using a multiclamp 700B amplifier (Molecular Devices) filtered at 5 kHz and sampled at 20 kHz with Digidata 1550B.

For PPR recordings, the cell membrane potential was held at −70 mV, and IPSCs in PoM were evoked by a 2-ms 473-nm light stimulation. Paired-pulse stimuli with an interstimulus interval of 50, 100, and 200 ms were applied. The PPR was calculated as the peak current that responded to the second pulse divided by that to the first pulse.

For light-evoked EPSC recordings, the cell membrane potential was held at −70 mV. EPSCs were evoked by a 2-ms 473-nm light stimulation and recorded for 10 min followed by bath application of 10 μM CNQX for an additional 10 min. Signals were low-pass–filtered at 5 kHz, sampled at 10 kHz, and analyzed offline.

Behavioral assays

Experiments were conducted during the light cycle (8:00 to 20:00). Mice were habituated to investigator handling for 1 to 2 min on three consecutive days. Handling took place in the holding room where the mice were housed. Before each handling session, mice were transported by wheeled cart to and from the vicinity of the behavior rooms to habituate them to the journey. All behavior experiments were analyzed blinded to the experimental groups. Given behavioral variability, assays were performed using a minimum of 6 to 10 mice per group to ensure adequate power for any observed differences. Brain sections were prepared to confirm efficient viral labeling in target areas following behavioral protocols. Animals lacking adequate labeling were excluded before behavior quantification.

Response to whisker stimulation

We performed the test as previously described (*18*). All experiments required one video camera, a home cage, an experimental cage, and a wooden stick. All formal experiments and habituation steps were conducted simultaneously between 1 hour after the onset of the light phase (8:00 to 18:00) and 1 hour before the dark phase. All recording equipment and experimental cages were placed in the same position during the entire experimental procedure. After each experiment, we used paper towels and 75% ethanol to clean the smell of the last experiment. Each mouse had its experimental cage. A handful of bedding for each mouse was introduced to the experimental cage a few days before the formal experiment to eliminate stress from the unfamiliar environment. The habituation phase was performed for 3 days before the experiment during which each mouse was introduced into the experimental cage with its own bedding for 30 min. The habituation phase was repeated on the experiment day, and a wooden stick was introduced into the cage. The mouse was not stimulated by the stick, which was shaking above the mouse for 5 min and referred as the sham phase for the animals habituating to the wooden stick application. Subsequently, we continuously stimulated the whiskers for 5 min for three consecutive rounds with a 1-min interval. The behavioral assessment was based on manual video scoring of single behaviors. Five different categories were scored; the behavioral responses analyzed were freezing (fearful behavior), stance (rearing and guarding), hyperventilation (overbreathing), aggressiveness (aggressive response to stick presentation), and evasiveness (escaping from the stick stimulation) on a qualitative scale of 0 to 2 points (0, absent; 1, scarcely present during the observation period; 2, present for most of the observation period). All the experimenters are blind to the experimental groups.

CFC test

The mice were adapted to the experimental environment the day before the formal test. Two different chambers were used. Chamber A (Vanbi, China) was a square chamber with an electrical grid floor to provide foot shock to the animals, and Chamber B (Vanbi, China) was a plastic tub (20 cm diameter, 30 cm height, rough surface). Thirteen days after SPS&S on day 14, each animal was placed in chamber A for 2 min for habituation. Next, a 30-s tone referred to CS (75 dB, 4500 Hz) and a foot shock referred to US (0.8 mA, 2 s) were performed in the last 2 s of tone stimulation. After the foot shock, there was a 60-s intertrial interval. CS and US were administered for 10 rounds in each trial. On day 15, the context test was conducted for which animals were first placed in chamber A for a 5-min exploration. After a 2-hour break, the cue test continued and the animals explored chamber B for 3 min and then were subjected to a 3-min conditioned tone (75 dB, 4500 Hz) without any

other stimulation. On day 21, the CFC test was performed again for 5 min for each mouse in contest A. "Freezing" behavior was defined as sustained immobility except for respiratory movements in a stereotypical crouching position for at least 1 s. When two CFC test sessions are needed in the optogenetic experiments, we followed an "off-on" rule as in a previous report (*41*). All behavioral assessments were video-recorded using Freezing Frame 3 (Vanbi, China) and analyzed using SMART v.3.0 software (Panlab Harvard Apparatus).

RNA sequencing

The mice were injected with retro-AAV-eGFP virus into PoM bilateral, and the PTSD establishment was conducted 1 week later. On the 14th day after PTSD establishment, the tissue of TRN was microdissected from normal and PTSD mice rapidly on dry ice. Total RNA was extracted by using an RNAmini kit (Qiagen, Germany). Strand-specific libraries were constructed using a TruSeq RNA sample preparation kit (Illumina, San Diego, CA, USA), and sequencing was carried out using an Illumina Novaseq 6000 instrument by Novel Bioinformatics (Shanghai, China). The clean reads were then aligned to mouse genome (version GRCh38 NCBI) using hisat2. HTseq was used to count gene, and the expression of gene transcript was calculated by FPKM (fragments per kilobase of exon model per million mapped reads). Differential expression analysis was performed using DESeq algorithm under the criteria that fold change > 1.5 and false discovery rate (FDR) < 0.05. Then, the gene ontology (GO) analysis was performed: GO analysis was performed to facilitate elucidating the biological implications of unique genes in the significant or representative profiles of the target gene of the differentially expressed miRNA in the experiment (*64*). We downloaded the GO annotations from National Center for Biotechnology Information (NCBI; www.ncbi.nlm.nih.gov/), UniProt (www.uniprot.org/), and Gene Ontology (www.geneontology.org/). Fisher's exact test was applied to identify the significant GO categories, and FDR was used to correct the *P* value. Last, pathway analysis was committed: Pathway analysis was used to find out the significant pathway of the differential genes according to Kyoto Encyclopedia of Genes and Genomes (KEGG) database. We turn to the Fisher's exact test to select the significant pathway, and the threshold of significance was defined by *P* value and FDR (*65*).

Cell counting

Brain sections were imaged with a 10× magnification objective on a confocal microscope (FV3000, Olympus, Japan) or fluorescence microscope (VS200, Olympus, Japan). Images were processed using ImageJ, and quantifications were performed manually from three to five sections per animal. For spine analysis, we collected 8 to 10 spines from one slice and counted 10 slices from three control mice and 11 slices from three PTSD mice. All counting experiments were conducted blinded to the experimental group. Cell quantification among different parts of this study could be found in table S2.

Statistical analyses

All analysis was performed by investigators blinded to experimental groups. Statistical analyses were performed using Prism v.6.0 (GraphPad Software Inc.) and SPSS v.21.0. No statistical methods were used to predetermine sample sizes. The normality test was performed by the Shapiro-Wilk test. The homogeneity of variance test was performed by Levene's test. Data that met these two conditions were analyzed using a two-tailed unpaired or paired *t* test, one-factor analysis of variance (ANOVA), and two-way ANOVA. Datasets that were not normally distributed were analyzed with a nonparametric test. Values are expressed as means ± SEM. All behavioral, electrophysiological, biochemical, and morphological data were obtained by counterbalancing experimental conditions with controls, except for optogenetic experiments of CFC tests. Details of particular statistical analyses can be found in table S1. Statistical significance was accepted when $P < 0.05$.

Supplementary Materials

This PDF file includes:
Figs. S1 to S18
Tables S1 to S3

Other Supplementary Material for this manuscript includes the following:
Movie S1

View/request a protocol for this paper from *Bio-protocol*.

REFERENCES AND NOTES

1. R. J. Fenster, L. A. M. Lebois, K. J. Ressler, J. Suh, Brain circuit dysfunction in post-traumatic stress disorder: From mouse to man. *Nat. Rev. Neurosci.* **19**, 535–551 (2018).
2. M. Purgato, C. Gastaldon, D. Papola, M. van Ommeren, C. Barbui, W. A. Tol, Psychological therapies for the treatment of mental disorders in low- and middle-income countries affected by humanitarian crises. *Cochrane Database Syst. Rev.* **7**, CD011849 (2018).
3. F. Cathomas, L. M. Holt, E. M. Parise, J. Liu, J. W. Murrough, P. Casaccia, E. J. Nestler, S. J. Russo, Beyond the neuron: Role of non-neuronal cells in stress disorders. *Neuron* **110**, 1116–1138 (2022).
4. A. Fratzl, A. M. Koltchev, N. Vissers, Y. L. Tan, A. Marques-Smith, A. V. Stempel, T. Branco, S. B. Hofer, Flexible inhibitory control of visually evoked defensive behavior by the ventral lateral geniculate nucleus. *Neuron* **109**, 3810–3822.e9 (2021).
5. Y. T. Tseng, B. Zhao, S. Chen, J. Ye, J. Liu, L. Liang, H. Ding, B. Schaefke, Q. Yang, L. Wang, F. Wang, L. Wang, The subthalamic corticotropin-releasing hormone neurons mediate adaptive REM-sleep responses to threat. *Neuron* **110**, 1223–1239.e8 (2022).
6. G. J. Kirouac, The paraventricular nucleus of the thalamus as an integrating and relay node in the brain anxiety network. *Front. Behav. Neurosci.* **15**, 627633 (2021).
7. M. Q. La-Vu, E. Sethi, S. Maesta-Pereira, P. J. Schuette, B. C. Tobias, F. Reis, W. Wang, A. Torossian, A. Bishop, S. J. Leonard, L. Lin, C. M. Cahill, A. Adhikari, Sparse genetically defined neurons refine the canonical role of periaqueductal gray columnar organization. *eLife* **11**, e77115 (2022).
8. M. B. Pardi, J. Vogenstahl, T. Dalmay, T. Spanò, D. L. Pu, L. B. Naumann, F. Kretschmer, H. Sprekeler, J. J. Letzkus, A thalamocortical top-down circuit for associative memory. *Science* **370**, 844–848 (2020).
9. R. Naim, S. P. Haller, J. O. Linke, A. Jaffe, J. Stoddard, M. Jones, A. Harrewijn, K. Kircanski, Y. Bar-Haim, M. A. Brotman, Context-dependent amygdala-prefrontal connectivity during the dot-probe task varies by irritability and attention bias to angry faces. *Neuropsychopharmacology* **47**, 2283–2291 (2022).
10. M. M. Halassa, L. Acsády, Thalamic inhibition: Diverse sources, diverse scales. *Trends Neurosci.* **39**, 680–693 (2016).
11. S. El-Boustani, B. S. Sermet, G. Foustoukos, T. B. Oram, O. Yizhar, C. C. H. Petersen, Anatomically and functionally distinct thalamocortical inputs to primary and secondary mouse whisker somatosensory cortices. *Nat. Commun.* **11**, 3342 (2020).
12. M. Barbier, S. Croizier, G. Alvarez-Bolado, P. Y. Risold, The distribution of Dlx1-2 and glutamic acid decarboxylase in the embryonic and adult hypothalamus reveals three differentiated LHA subdivisions in rodents. *J. Chem. Neuroanat.* **121**, 102089 (2022).
13. D. Baez-Nieto, A. Allen, S. Akers-Campbell, L. Yang, N. Budnik, A. Pupo, Y. C. Shin, G. Genovese, M. Liao, E. Pérez-Palma, H. Heyne, D. Lal, D. Lipscombe, J. Q. Pan, Analysing an allelic series of rare missense variants of CACNA1I in a Swedish schizophrenia cohort. *Brain* **145**, 1839–1853 (2022).
14. M. Nakajima, L. I. Schmitt, G. Feng, M. M. Halassa, Combinatorial targeting of distributed forebrain networks reverses noise hypersensitivity in a model of autism spectrum disorder. *Neuron* **104**, 488–500.e11 (2019).

15. M. F. Wells, R. D. Wimmer, L. I. Schmitt, G. Feng, M. M. Halassa, Thalamic reticular impairment underlies attention deficit in Ptchd1(Y/−) mice. *Nature* **532**, 58–63 (2016).
16. P. Dong, H. Wang, X. F. Shen, P. Jiang, X. T. Zhu, Y. Li, J. H. Gao, S. Lin, Y. Huang, X. B. He, F. Q. Xu, S. Duan, H. Lian, H. Wang, J. Chen, X. M. Li, A novel cortico-intrathalamic circuit for flight behavior. *Nat. Neurosci.* **22**, 941–949 (2019).
17. K. Xi, X. Huang, T. Liu, Y. Liu, H. Mao, M. Wang, D. Feng, W. Wang, B. Guo, S. Wu, Translational relevance of behavioral, neural, and electroencephalographic profiles in a mouse model of post-traumatic stress disorder. *Neurobiol. Stress* **15**, 100391 (2021).
18. G. Chelini, V. Zerbi, L. Cimino, A. Grigoli, M. Markicevic, F. Libera, S. Robbiati, M. Gadler, S. Bronzoni, S. Miorelli, A. Galbusera, A. Gozzi, S. Casarosa, G. Provenzano, Y. Bozzi, Aberrant somatosensory processing and connectivity in mice lacking engrailed-2. *J. Neurosci.* **39**, 1525–1538 (2019).
19. M. J. Wall, D. R. Collins, S. L. Chery, Z. D. Allen, E. D. Pastuzyn, A. J. George, V. D. Nikolova, S. S. Moy, B. D. Philpot, J. D. Shepherd, J. Müller, M. D. Ehlers, A. M. Mabb, S. A. L. Corrêa, The temporal dynamics of arc expression regulate cognitive flexibility. *Neuron* **98**, 1124–1132.e7 (2018).
20. L. F. Gumy, E. A. Katrukha, I. Grigoriev, D. Jaarsma, L. C. Kapitein, A. Akhmanova, C. C. Hoogenraad, MAP2 defines a pre-axonal filtering zone to regulate KIF1- versus KIF5-dependent cargo transport in sensory neurons. *Neuron* **94**, 347–362.e7 (2017).
21. D. Ulrich, J. R. Huguenard, Purinergic inhibition of GABA and glutamate release in the thalamus: Implications for thalamic network activity. *Neuron* **15**, 909–918 (1995).
22. O. Yizhar, L. E. Fenno, M. Prigge, F. Schneider, T. J. Davidson, D. J. O'Shea, V. S. Sohal, I. Goshen, J. Finkelstein, J. T. Paz, K. Stehfest, R. Fudim, C. Ramakrishnan, J. R. Huguenard, P. Hegemann, K. Deisseroth, Neocortical excitation/inhibition balance in information processing and social dysfunction. *Nature* **477**, 171–178 (2011).
23. C. J. Guenthner, K. Miyamichi, H. H. Yang, H. C. Heller, L. Luo, Permanent genetic access to transiently active neurons via TRAP: Targeted recombination in active populations. *Neuron* **78**, 773–784 (2013).
24. M. Aime, E. Augusto, V. Kouskoff, T. Campelo, C. Martin, Y. Humeau, N. Chenouard, F. Gambino, The integration of Gaussian noise by long-range amygdala inputs in frontal circuit promotes fear learning in mice. *eLife* **9**, e62594 (2020).
25. D. I. Choi, J. Kim, H. Lee, J. I. Kim, Y. Sung, J. E. Choi, S. J. Venkat, P. Park, H. Jung, B. K. Kaang, Synaptic correlates of associative fear memory in the lateral amygdala. *Neuron* **109**, 2717–2726.e3 (2021).
26. K. J. Ressler, S. Berretta, V. Y. Bolshakov, I. M. Rosso, E. G. Meloni, S. L. Rauch, W. A. Carlezon Jr., Post-traumatic stress disorder: Clinical and translational neuroscience from cells to circuits. *Nat. Rev. Neurol.* **18**, 273–288 (2022).
27. R. Yehuda, J. LeDoux, Response variation following trauma: A translational neuroscience approach to understanding PTSD. *Neuron* **56**, 19–32 (2007).
28. I. Liberzon, J. L. Abelson, Context processing and the neurobiology of post-traumatic stress disorder. *Neuron* **92**, 14–30 (2016).
29. J. E. Dunsmoor, J. M. Cisler, G. A. Fonzo, S. K. Creech, C. B. Nemeroff, Laboratory models of post-traumatic stress disorder: The elusive bridge to translation. *Neuron* **110**, 1754–1776 (2022).
30. P. R. Zoladz, C. R. Park, M. Fleshner, D. M. Diamond, Psychosocial predator-based animal model of PTSD produces physiological and behavioral sequelae and a traumatic memory four months following stress onset. *Physiol. Behav.* **147**, 183–192 (2015).
31. C. L. Wellman, M. Camp, V. M. Jones, K. P. MacPherson, J. Ihne, P. Fitzgerald, M. Maroun, E. Drabant, R. Bogdan, A. R. Hariri, A. Holmes, Convergent effects of mouse Pet-1 deletion and human PET-1 variation on amygdala fear and threat processing. *Exp. Neurol.* **250**, 260–269 (2013).
32. D. Y. Feng, B. L. Guo, G. H. Liu, K. Xu, J. Yang, K. Tao, J. Huang, L. Y. Wang, W. Wang, S. X. Wu, Nerve growth factor against PTSD symptoms: Preventing the impaired hippocampal cytoarchitectures. *Prog. Neurobiol.* **184**, 101721 (2020).
33. M. M. Halassa, S. M. Sherman, Thalamocortical circuit motifs: A general framework. *Neuron* **103**, 762–770 (2019).
34. J. Jaramillo, J. F. Mejias, X. J. Wang, Engagement of pulvino-cortical feedforward and feedback pathways in cognitive computations. *Neuron* **101**, 321–336.e9 (2019).
35. A. W. Huang, A. D. Barber, Development of lateral pulvinar resting state functional connectivity and its role in attention. *Cortex* **136**, 77–88 (2021).
36. R. A. Lanius, P. C. Williamson, J. Hopper, M. Densmore, K. Boksman, M. A. Gupta, R. W. Neufeld, J. S. Gati, R. S. Menon, Recall of emotional states in posttraumatic stress disorder: An fMRI investigation. *Biol. Psychiatry* **53**, 204–210 (2003).
37. P. Neumeister, K. Feldker, C. Y. Heitmann, R. Helmich, B. Gathmann, M. P. I. Becker, T. Straube, Interpersonal violence in posttraumatic women: Brain networks triggered by trauma-related pictures. *Soc. Cogn. Affect. Neurosci.* **12**, 555–568 (2017).
38. C. C. Petersen, The functional organization of the barrel cortex. *Neuron* **56**, 339–355 (2007).
39. Z. Zhu, Q. Ma, L. Miao, H. Yang, L. Pan, K. Li, L. H. Zeng, X. Zhang, J. Wu, S. Hao, S. Lin, X. Ma, W. Mai, X. Feng, Y. Hao, L. Sun, S. Duan, Y. Q. Yu, A substantia innominata-midbrain circuit controls a general aggressive response. *Neuron* **109**, 1540–1553.e9 (2021).
40. C. R. de Carvalho, M. W. Lopes, L. C. Constantino, A. A. Hoeller, H. M. de Melo, R. Guarnieri, M. N. Linhares, Z. A. Bortolotto, R. D. Prediger, A. Latini, K. Lin, J. Licinio, R. B. Leal, R. Walz, The ERK phosphorylation levels in the amygdala predict anxiety symptoms in humans and MEK/ERK inhibition dissociates innate and learned defensive behaviors in rats. *Mol. Psychiatry* **26**, 7257–7269 (2021).
41. P. Tovote, M. S. Esposito, P. Botta, F. Chaudun, J. P. Fadok, M. Markovic, S. B. Wolff, C. Ramakrishnan, L. Fenno, K. Deisseroth, C. Herry, S. Arber, A. Luthi, Midbrain circuits for defensive behaviour. *Nature* **534**, 206–212 (2016).
42. X. Zhang, J. Kim, S. Tonegawa, Amygdala reward neurons form and store fear extinction memory. *Neuron* **105**, 1077–1093.e7 (2020).
43. M. F. Barbano, H. L. Wang, S. Zhang, J. Miranda-Barrientos, D. J. Estrin, A. Figueroa-González, B. Liu, D. J. Barker, M. Morales, VTA glutamatergic neurons mediate innate defensive behaviors. *Neuron* **107**, 368–382.e8 (2020).
44. Z. Zhou, X. Liu, S. Chen, Z. Zhang, Y. Liu, Q. Montardy, Y. Tang, P. Wei, N. Liu, L. Li, R. Song, J. Lai, X. He, C. Chen, G. Bi, G. Feng, F. Xu, L. Wang, A VTA GABAergic neural circuit mediates visually evoked innate defensive responses. *Neuron* **103**, 473–488.e6 (2019).
45. L. Huang, T. Yuan, M. Tan, Y. Xi, Y. Hu, Q. Tao, Z. Zhao, J. Zheng, Y. Han, F. Xu, M. Luo, P. J. Sollars, M. Pu, G. E. Pickard, K. F. So, C. Ren, A retinoraphe projection regulates serotonergic activity and looming-evoked defensive behaviour. *Nat. Commun.* **8**, 14908 (2017).
46. R. I. Martinez-Garcia, B. Voelcker, J. B. Zaltsman, S. L. Patrick, T. R. Stevens, B. W. Connors, S. J. Cruikshank, Two dynamically distinct circuits drive inhibition in the sensory thalamus. *Nature* **583**, 813–818 (2020).
47. A. Krol, R. D. Wimmer, M. M. Halassa, G. Feng, Thalamic reticular dysfunction as a circuit endophenotype in neurodevelopmental disorders. *Neuron* **98**, 282–295 (2018).
48. A. Young, R. D. Wimmer, Implications for the thalamic reticular nucleus in impaired attention and sleep in schizophrenia. *Schizophr. Res.* **180**, 44–47 (2017).
49. S. Parnaudeau, P. K. O'Neill, S. S. Bolkan, R. D. Ward, A. I. Abbas, B. L. Roth, P. D. Balsam, J. A. Gordon, C. Kellendonk, Inhibition of mediodorsal thalamus disrupts thalamofrontal connectivity and cognition. *Neuron* **77**, 1151–1162 (2013).
50. J. H. Lee, C. V. Latchoumane, J. Park, J. Kim, J. Jeong, K. H. Lee, H. S. Shin, The rostroventral part of the thalamic reticular nucleus modulates fear extinction. *Nat. Commun.* **10**, 4637 (2019).
51. X. Wang, X. Chou, B. Peng, L. Shen, J. J. Huang, L. I. Zhang, H. W. Tao, A cross-modality enhancement of defensive flight via parvalbumin neurons in zona incerta. *eLife* **8**, e42728 (2019).
52. H. Wang, P. Dong, C. He, X. Y. Feng, Y. Huang, W. W. Yang, H. J. Gao, X. F. Shen, S. Lin, S. X. Cao, H. Lian, J. Chen, M. Yan, X. M. Li, Incerta-thalamic circuit controls nocifensive behavior via cannabinoid type 1 receptors. *Neuron* **107**, 538–551.e7 (2020).
53. C. Bennett, S. D. Gale, M. E. Garrett, M. L. Newton, E. M. Callaway, G. J. Murphy, S. R. Olsen, Higher-order thalamic circuits channel parallel streams of visual information in mice. *Neuron* **102**, 477–492.e5 (2019).
54. P. G. Anastasiades, D. P. Collins, A. G. Carter, Mediodorsal and ventromedial thalamus engage distinct L1 circuits in the prefrontal cortex. *Neuron* **109**, 314–330.e4 (2021).
55. Y. B. Saalmann, S. Kastner, Cognitive and perceptual functions of the visual thalamus. *Neuron* **71**, 209–223 (2011).
56. R. A. Mease, M. Metz, A. Groh, Cortical sensory responses are enhanced by the higher-order thalamus. *Cell Rep.* **14**, 208–215 (2016).
57. K. S. Rommelfanger, S. J. Jeong, A. Ema, T. Fukushi, K. Kasai, K. M. Ramos, A. Salles, I. Singh, Neuroethics questions to guide ethical research in the international brain initiatives. *Neuron* **100**, 19–36 (2018).
58. V. J. Sydnor, B. Larsen, D. S. Bassett, A. Alexander-Bloch, D. A. Fair, C. Liston, A. P. Mackey, M. P. Milham, A. Pines, D. R. Roalf, J. Seidlitz, T. Xu, A. Raznahan, T. D. Satterthwaite, Neurodevelopment of the association cortices: Patterns, mechanisms, and implications for psychopathology. *Neuron* **109**, 2820–2846 (2021).
59. L. Huang, Q. W. Pan, H. X. Hu, X. Y. Xu, Identification of the status of individual drug-administration behavior in heroin-withdrawal rats based on FrA EEG. *Chin. J. Appl. Physiol.* **36**, 517–523 (2020).
60. C. S. Lai, T. F. Franke, W. B. Gan, Opposite effects of fear conditioning and extinction on dendritic spine remodelling. *Nature* **483**, 87–91 (2012).
61. N. Tamamaki, Y. Yanagawa, R. Tomioka, J. Miyazaki, K. Obata, T. Kaneko, Green fluorescent protein expression and colocalization with calretinin, parvalbumin, and somatostatin in the GAD67-GFP knock-in mouse. *J. Comp. Neurol.* **467**, 60–79 (2003).
62. B. Guo, J. Chen, Q. Chen, K. Ren, D. Feng, H. Mao, H. Yao, J. Yang, H. Liu, Y. Liu, F. Jia, C. Qi, T. Lynn-Jones, H. Hu, Z. Fu, G. Feng, W. Wang, S. Wu, Anterior cingulate cortex dysfunction underlies social deficits in Shank3 mutant mice. *Nat. Neurosci.* **22**, 1223–1234 (2019).

63. Z. Z. Li, W. J. Han, Z. C. Sun, Y. Chen, J. Y. Sun, G. H. Cai, W. N. Liu, T. Z. Wang, Y. D. Xie, H. H. Mao, F. Wang, S. B. Ma, F. D. Wang, R. G. Xie, S. X. Wu, C. Luo, Extracellular matrix protein laminin β1 regulates pain sensitivity and anxiodepression-like behaviors in mice. *J. Clin. Invest.* **131**, (2021).
64. M. Ashburner, C. A. Ball, J. A. Blake, D. Botstein, H. Butler, J. M. Cherry, A. P. Davis, K. Dolinski, S. S. Dwight, J. T. Eppig, M. A. Harris, D. P. Hill, L. Issel-Tarver, A. Kasarskis, S. Lewis, J. C. Matese, J. E. Richardson, M. Ringwald, G. M. Rubin, G. Sherlock, Gene ontology: Tool for the unification of biology. The Gene Ontology Consortium. *Nat. Genet.* **25**, 25–29 (2000).
65. S. Draghici, P. Khatri, A. L. Tarca, K. Amin, A. Done, C. Voichita, C. Georgescu, R. Romero, A systems biology approach for pathway level analysis. *Genome Res.* **17**, 1537–1545 (2007).

Acknowledgments: We thank K. Ren, F. Liu, and J. Li for technical assistance and all the laboratory members for helpful discussion. We thank scientificmanuscripteditting.com for language editing. **Funding:** This work was supported by the Science and Technology Innovation 2030 Project of China (2021ZD0201005 to S.W.); the Natural Science Foundation of China (82221001, 81730035 to S.W., 82201699 to B.G. and 82071536 to W.W.); Natural Science Basic Research Program of Shaanxi (2021JCW-13 to S.W.); Key Laboratory of Neural and Vascular Biology, Ministry of Education of China (NV202100012 to B.G.); Young Talent Fund of University Association for Science and Technology in Shaanxi (20220306 to B.G.); and Postdoctoral Innovation Talents Support Program of China (to B.G.). **Author contributions:** K.X., B.G., and S.W. conceived and designed the study. K.X., H.X., X.H., and Z.Y. performed the behavior tests. K.X., X.H., M.L., and H.L. performed virus injection and histochemistry experiments. H.X. performed the in vitro Ephys experiments. K.X., H.M., G.M., Z.C., and Y.X. analyzed data. Y.L., W.W., and D.F. provided technical assistance. B.G. and S.W. provided funding and supervised the work. K.X., H.X., X.H., and B.G. wrote the manuscript with inputs from all authors. **Competing interests:** The authors declare that they have no competing interests. **Data and materials availability:** All data needed to evaluate the conclusions in the paper are present in the paper and/or the Supplementary Materials.

Submitted 26 August 2022
Accepted 3 January 2023
Published 3 February 2023
10.1126/sciadv.ade5987